Floquet-Theory-based Small-Signal Stability Analysis of Single-Phase Asymmetric Multilevel Inverters with SRF Voltage Control

Han, Y.; Lin, X.; Fang, X.; Xu, L.; Yang, P.; Hu, W.; Coelho, E. A.; Blaabjerg, F.

Published in:
IEEE Transactions on Power Electronics

DOI (link to publication from Publisher):
10.1109/TPEL.2019.2930326

Publication date:
2020

Document Version
Accepted author manuscript, peer reviewed version

This article has been accepted for publication in a future issue of this journal, but has not been fully edited. Content may change prior to final publication. Citation information: DOI 10.1109/TPEL.2019.2930326, IEEE Transactions on Power Electronics

Floquet-Theory-based Small-Signal Stability Analysis of Single-Phase Asymmetric Multilevel Inverters with SRF Voltage Control

Yang Han, *Senior Member, IEEE*, Xiangyang Lin, Xu Fang, Lin Xu, Ping Yang, Weihao Hu, *Senior Member, IEEE*
Ernane A.A. Coelho and Frede Blaabjerg, *Fellow, IEEE*

***Abstract*- This paper proposes a small-signal model and Floquet theory-based method for analyzing small-signal stability of a single-phase asymmetric cascaded H-bridge multilevel inverter (ACHMI) operating in stand-alone mode. The studied ACHMI system consists of the power stage and cascaded control loops, which includes the voltage loop in the synchronous reference frame (SRF), capacitor current feedback control and hybrid modulation scheme. Due to the SRF voltage control, the derived small-signal model under linear and nonlinear load conditions are inherently periodically time-variant. Therefore, the Floquet theory is employed to analyze the stability regions of the dual-loop control parameters of the ACHMI. Furthermore, the loci and moduli of Floquet multipliers are calculated to accurately evaluate the respective effects of control parameters on the stability of the system. With the stability analysis based on the small-signal model and Floquet theory-based method, an effective selection range of control parameters of the multilevel inverter can be obtained. Finally, the experimental results from a reduced-scale laboratory prototype ACHMI are presented to validate the theoretical analysis, and the effectiveness of proposed analysis method in high-power applications is verified by the simulation results from a 10kV medium-voltage ACHMI.**

***Index Terms*—Multilevel inverter, small-signal modelling, hybrid modulation, SRF voltage control, stability region**

I. INTRODUCTION

The cascaded H-bridge multilevel inverter (CHMI) is an efficient solution for various high-power applications, such as renewable energy generation systems, DC transmission systems, flexible AC transmission systems (FACTS), AC drive systems, etc., [1-3]. Compared to the traditional two-level inverter, the neutral-point-clamped (NPC) inverters, and flying-capacitor (FC) inverters, the CHMI demonstrates remarkable merits in several aspects, i.e., the quality of output voltage, the capability extension of the inverters, and the convenience of modularization [4-7]. Moreover, the feature of modularity not only increases the reliability of the device, but also makes the multilevel inverters an attractive choice for new applications [8]. There are varieties of multilevel inverters topologies such as capacitor-clamped [9], diode clamped [10], and modular cascaded [11]. But in practical applications, two CHMI topologies are usually applied. One is the symmetrical CHMI (SCHMI), named owing to the same dc-bus voltage of each H-bridge unit, and the other is called the asymmetrical CHMI (ACHMI), which has different dc-link bus voltages for its H-bridge units. The superiority of configuring the different dc-link bus voltages among the individual H-bridge units is that, more stairs in the total terminal voltages can be produced with a given number of H-bridge units, and results in a higher number of output voltage levels. The dc-link bus voltages of the H-bridge units in ACHMI topology is normally set in a certain ratio, such as 1:2:4:.., 1:3:9:.., and 1:2:6:.., etc., [2, 12].

Like the two-level inverters, multilevel inverters can work in the grid-connected mode or stand-alone mode, and the control strategies for these two modes are almost the same as those for the two-level inverters. It is well-known that LC output filters are normally used in inverters operating in the stand-alone mode, and the inverters in the stand-alone mode are employed to feed different loads including linear and nonlinear load. Those inverters often are controlled by single voltage closed-loop, or dual closed-loops composed of outer voltage loop and inner current loop. For the inner current loop of the single-phase inverter systems, proportional control is commonly used, due to its simplicity and great dynamic response. While for the outer voltage loops or single voltage regulator, a variety of control methods can be applied, such as the proportional-resonant (PR) control, repetitive control, deadbeat control, and sliding mode control [13, 14]. However, a generalized proportional integral (GPI) controller is used for single-phase multilevel inverter in [15], which shows the robustness of the output voltage regulation and output trajectory tracking. In addition to these frequently used control methodologies, the proportional-integral (PI) control scheme in the synchronous reference frame (SRF) was adopted by some researchers because of the remarkable dynamic performance [16]. By employing the orthogonal-signal-generation (OSG) techniques and time-delay module, a virtual second phase signal is produced. This method makes the single-phase inverter system mimic a two-phase system in the SRF, such that the traditional PI controllers can be used to achieve the zero steady-state error with an excellent dynamic performance for the voltage control of single-phase

Manuscript received December 04, 2018; revised March 17, 2019 and June 03, 2019; accepted July 17, 2019. Date of publication *******; date of current version *******. This work was supported in part by the National Natural Science Foundation of China under grant 51307015, in part by Sichuan Province Key Research and Development Project under grant 2017GZ0347, in part by Natural Science Foundation of Guangdong Province under grant 2018A030313494, and in part by the State Key Laboratory of Alternate Electrical Power System with Renewable Energy Sources under grant LAPS18007. Recommended for publication by Associate Editor *****.

Y. Han, X. Lin, P. Yang and W. Hu are with the School of Mechanical and Electrical Engineering, University of Electronic Science and Technology of China, Chengdu 611731, China (e-mail: hanyang@uestc.edu.cn; 1014176020@qq.com; ping@uestc.edu.cn; whu@uestc.edu.cn).

X. Fang is with ZTE corporation, ZTE Industrial Park, Shenzhen 518057, China (Xulinks@126.com)

L. Xu is with the Sichuan Electric Power Research Institute, Sichuan Electric Power Company, Chengdu 610072, China (xulinn@163.com).

E. A. A. Coelho is with the Universidade Federal de Uberlandia, Uberlandia 38400-902, Brazil (e-mail: ernane@ufu.br).

F. Blaabjerg is with Department of Energy Technology, Aalborg University, 9220 Aalborg, Denmark (e-mail: fbl@et.aau.dk).

Color versions of one or more of the figures in this paper are available online at http://ieeexplore.ieee.org.

Digital Object Identifier ******/TPEL.*******

This article has been accepted for publication in a future issue of this journal, but has not been fully edited. Content may change prior to final publication. Citation information: DOI 10.1109/TPEL.2019.2930326, IEEE Transactions on Power Electronics

inverters. Therefore, the voltage control method based on the SRF-PI controller is adopted for the studied single-phase ACHMI in this paper.

Meanwhile, the pulse-width modulation scheme is another fundamental and important part for the multilevel inverter control stage. The most common modulation schemes for the multilevel inverters include the level-shift (LS) PWM, phase-shift (PS) PWM, space-vector PWM (SVM), pre-programmed PWM, staircase modulation (also known as nearest-level modulation) [12], and the hybrid modulation (HM) scheme. In practical applications, staircase modulation and hybrid modulation methods are normally applied for the ACHMI topology [17]. The classical staircase modulation is presented in detail in [12, 17]. Furthermore, the impact on input and output harmonics, the analysis and the application of HM scheme can be found in [18, 19, 20], respectively.

Currently, the studies on multilevel inverter systems mainly focuses on power-stage topologies, modulation strategies, dc-bus voltage control schemes, and power distribution of the sub-modules in the steady-state conditions [21, 22], and most of them are conducted based on the open-loop control and switching function descriptions [12], which are normally unsuitable for the system stability analysis and parameter design. A *z*-domain model based on small signal transfer function for the multilevel inverter is derived in [23], which is used to select parameters reasonably and improve the control performance. Then, several literatures present studies of the system modeling, the control strategies, the parameter design and the stability analysis of the multilevel inverter systems in the framework of the closed-loop control schemes [24, 25]. Referring to the reported research, it can be concluded that there is no essential difference between the multilevel inverters and the two-level inverters in the system analysis when the closed-loop control is considered. Thus, the analysis methods for the two-level inverter systems can be extended to study multilevel inverter systems, including the widely applied small-signal analysis method [26].

In retrospect, the small-signal analysis method is first proposed in the researches of DC systems such as the Boost converter, and then, generalized into the studies of the 3-phase AC systems. The classical small-signal model is established through linearizing the system equations by adding perturbation components around the fixed DC operating point [27]. For the balanced three-phase AC case, the system can be first transformed into the *dq* reference frame, where the quantities are in DC forms, and then the modeling is performed as the same with the case in DC system. The classic small-signal model is generally linear and time-invariant, and can be represented as the homogeneous differential equations, where the system stability is determined by coefficient matrix. According to the classical control theory, the system is supposed to be stable only when all the eigenvalue loci of the coefficient matrix lie in the left-half complex plane. However, for the single-phase or unbalanced three-phase inverter systems, the steady-state AC variables cannot be directly converted into the DC forms through the coordinate transformation, but they have the periodic steady-state operating trajectories, which can be applied for establishing the small-signal model.

In addition, the differential equations of inverter systems could be linear or nonlinear, time-invariant or time-variant. For the single-phase and unbalanced three-phase inverter systems described by the nonlinear differential equations, the harmonic balance method is usually employed to figure out the periodic steady state operating trajectories, around which the small perturbation is subsequently applied to linearize and obtain the small-signal models. In this scenario, the obtained small-signal models are normally periodic and time-variant, hence the system stability can be analyzed by the Floquet or linear time periodic (LTP) theory [28, 29]. In case of the single-phase and unbalanced 3-phase inverter systems that represented by linear time-invariant differential equations, the small-signal modeling and stability analysis can be implemented at the vicinity of the hypothetical steady-state operating trajectories, where the differences between the steady-state solutions are neglected. The stability of linear time-invariant systems can be characterized by both small-signal model and transfer functions (or transfer function matrices), which are equivalent and they are interchangeable. However, for the periodically time-variant small-signal models, it cannot be converted from the system transfer functions or transfer function matrices directly. Hence, for those inverter systems represented by linear time-variant differential equations, the small-signal modeling can be performed around the hypothetical steady-state operating trajectories, and the stability can be precisely evaluated by the Floquet theory.

It is worth noting that, some researches introduce the small-signal method into the modeling of the partial loops in inverter systems [26, 30, 31]. Literatures [30] and [31] report the small-signal models of the PWM process, which are more effective in predicting the instabilities in converters. In [26], a small-signal model of the staircase modulation is proposed for a single-phase ACHMI system, where the small-signal perturbations are added to the open-loop modulation signals, and the control parameters are subsequently designed by using the transfer functions of the single and dual closed-loop control strategies. However, the small-signal model in [26] is a transfer function loop of the staircase modulation, rather than the model of whole system, thus the derivation of complete model needs to be further studied. In [32], stability analysis of single-phase inverter with SRF voltage control has been studied, and the small signal model of single-phase inverter with output LC filter has been built using both Jacobian matrix and Lyapunov exponent method, where the linear and nonlinear load conditions are also considered.

In this paper, a complete small-signal model including the power stage and control system is derived for a single-phase ACHMI system composed of three H-bridge cells and the dc-bus voltages ratio of 1:2:6. The presented control strategy contains dual closed-loop control loops and the hybrid modulation, where the voltage control loop of the ACHMI is achieved by using the PI controllers in the SRF. Small-signal models under different load conditions are obtained by the hypothetical steady state operating trajectories due to the time-variant system characteristic. Next, the stability regions of the fundamental and harmonic control parameters of the ACHMI system are evaluated in detail by using small-signal model and the Floquet theory-based method, hence the selection range of control parameters can be obtained. Moreover, the validity of the small-signal model and the feasibility of the proposed theoretical analysis method are verified by the experimental results. Finally, the proposed analysis method is extended to the ACHMI system with high

This article has been accepted for publication in a future issue of this journal, but has not been fully edited. Content may change prior to final publication. Citation information: DOI 10.1109/TPEL.2019.2930326, IEEE Transactions on Power Electronics

power level and verified by the simulation results

The rest of the paper is organized as follows. The description of the studied ACHMI system is presented in Section II. Section III introduces the detailed small-signal modeling and stability analysis method based on the Floquet theory. Then, five case studies are discussed in Section IV, where the stability regions of the fundamental and harmonic control parameters are analyzed by Floquet theory. In addition, the selection range of control parameter is discussed according to the stability analysis based on Floquet theory. In Section V, the experimental results obtained from the laboratory prototype is provided to validate the effectiveness of the theoretical analysis. Finally, the effectiveness of analysis method under the condition of high-power level ACHMI is verified in Section VI and the main conclusion is summarized in Section VII.

II. System Description of the ACHMI

In order to establish a general small-signal model of the single phase ACHMI system, the structure of inverter with output LC filter has been adopted and the similar structure can be found in [32]. The complete structure of the studied single-phase ACHMI system is shown in Fig. 1.

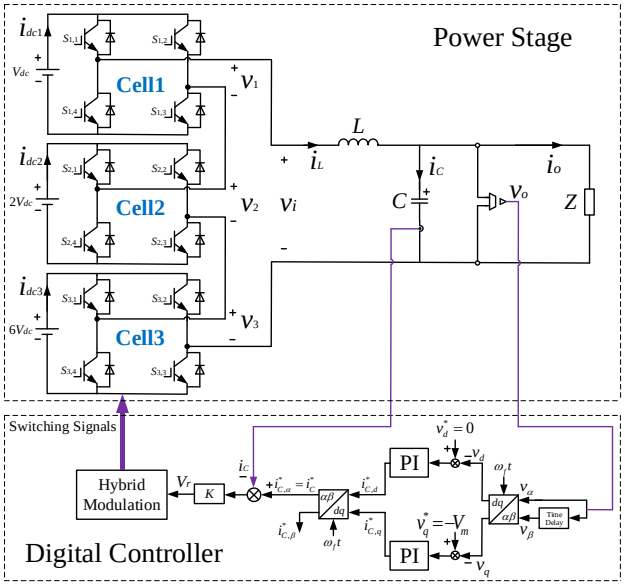

Fig. 1. System structure of the ACHMI system with SRF-based dual-loop control scheme.

It can be observed from Fig. 1 that the power-stage includes three cascaded H-bridge units, and the load is fed through the LC filter. The three H-bridge units, which possess the dc-bus voltages of V_{dc}, $2V_{dc}$ and $6V_{dc}$, are normally called low voltage, medium voltage and high voltage cell, respectively. The criterion for the dc-bus voltage setup has been discussed in detail in [12], which requires that the dc-bus voltage ratio k_1:k_2:k_3…:k_n in an ACHMI topology with n H-bridge cells must satisfy:

$$k_1 = 1,\ \ k_n = 2\sum_{i=1}^{n-1} k_i, n \geq 2 \tag{1}$$

Therefore, the maximum stair number in the total terminal voltage can be written as:

$$N = (2\sum_{i=1}^{n} k_i) + 1 \tag{2}$$

Furthermore, according to (2), the presented ACHMI prototype system in this paper can generate maximum 19 stairs in the total terminal voltage.

The filter output voltage and capacitor current feedback control are adopted to form the dual closed-loops control in the inverter system. The control strategy is realized in a digital controller, where the sampling frequency is equal to the PWM frequency in the HM process. As mentioned earlier, the outer voltage control loop is achieved by using two identical PI regulators in the SRF, while a proportional regulator is employed in the inner current control loop. The reference signal of the output voltage v_o is defined as:

$$v_o^* = V_m \sin(\omega_f t) \tag{3}$$

where V_m represents the amplitude of the reference voltage and ω_f is the fundamental angular frequency in output voltage.

The output voltage v_o (v_α) is delayed to generate the virtual voltage signal v_β in a time delay module, where the time lag τ is set as $\pi/(2\times\omega_f)$. Simultaneously, the time lag τ is equal to one quarter of fundamental cycle of the reference voltage v_o^* since it ensures that the output v_β is orthogonal to v_α. When the inverter system operates in the steady-state condition, it is rational to consider that $v_\alpha = v_o^* = V_m \sin(\omega_f t)$, and $v_\beta = -V_m \cos(\omega_f t)$. Therefore, the references of d-axis and q-axis voltages in the SRF are derived as:

$$\begin{bmatrix} v_d^* \\ v_q^* \end{bmatrix} = \begin{bmatrix} \cos(\omega_f t) & \sin(\omega_f t) \\ -\sin(\omega_f t) & \cos(\omega_f t) \end{bmatrix} \begin{bmatrix} V_m \sin(\omega_f t) \\ -V_m \cos(\omega_f t) \end{bmatrix} = \begin{bmatrix} 0 \\ -V_m \end{bmatrix} \tag{4}$$

The scheme of the adopted HM is shown in Fig. 2, and the detailed HM process is shown in Fig. 3. It can be observed from Fig. 2 that the modulation signal V_{r3} (V_r) is compared with the constant dc signal $\pm h_2$ to generate the output voltage v_{m3} of Cell3, which has a three-level voltage waveform. V_{r2} is obtained by subtracting v_{m3} from V_{r3}. Similarly, the modulation signal V_{r2} is compared with another constant dc signal $\pm h_1$ to obtain the output voltage v_{m2} of Cell2. Then, the modulation signal V_{r1} is generated by subtracting v_{m2} from V_{r2}. However, V_{r1} is compared with two high frequency unit triangular carriers to generate the output voltage v_{m1}. The output signals v_{m3}, v_{m2} and v_{m1} of different Cell have the weight of 6, 2, and 1, respectively. Then, the total output voltage v_{mi} is synthesized by summing v_{m1}, v_{m2} and v_{m3}, as shown in Fig. 3. After analyzing the HM, it suggests that the maximized output level of ACHMI can be achieved through the adopted hybrid modulation process.

The dc voltage level h_2 and h_1 are selected in the way that the unmodulated part can be produced by Cell1 to avoid over-modulation [20]. Hence, the DC modulation signal h_n of the (n+1)-th H-bridge cell in the HM process can be written as:

$$h_n = \sum_{i=1}^{n} k_i \tag{5}$$

Subsequently, the DC modulation signals h_1 and h_2 in present case are obtained as:

$$h_1 = 1,\ \ h_2 = 3 \tag{6}$$

The process of unipolar PWM of the low voltage cell (Cell 1) is carried out in the digital controller. The approximate quantitative relations for the modulation signal V_{r1} and output terminal voltage v_1 can be obtained by averaging the switching states of the low voltage cell within one PWM cycle, which is written as:

$$v_1(n) \approx V_{r1}(n) \cdot V_{dc} \tag{7}$$

This article has been accepted for publication in a future issue of this journal, but has not been fully edited. Content may change prior to final publication. Citation information: DOI 10.1109/TPEL.2019.2930326, IEEE Transactions on Power Electronics

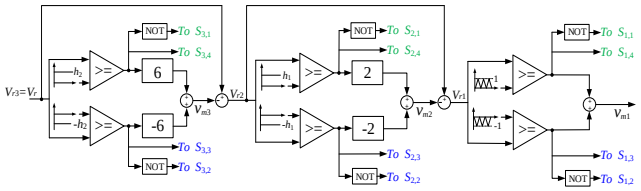

Fig. 2. Principle of hybrid modulation scheme for the ACHMI.

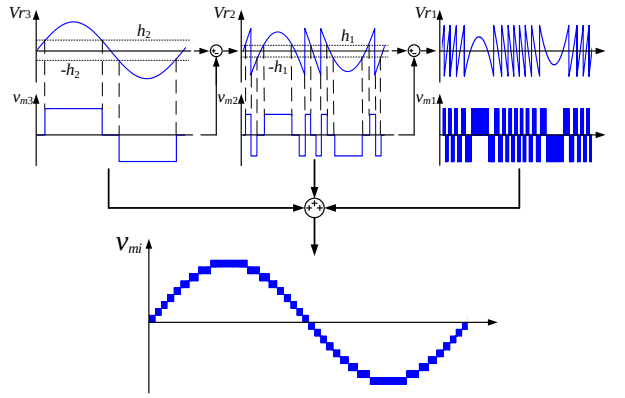

Fig. 3. The generation of the output terminal voltage waveforms of the ACHMI system.

Subsequently, in one PWM switching cycle, the total output terminal voltage v_i can be approximately expressed by the initial modulation signal V_r in a discrete form as:

$$v_i(n) \approx V_r(n) \cdot V_{dc} \tag{8}$$

Equation (8) represents the average model of the HM, which is seen as a gain loop in the mathematical expressions. Since the PWM cycle is normally quite small, the hybrid modulation can also be regarded as a proportional gain loop with the maximum $1.5T_s$ delay in continuous-time domain.

III. Small-Signal Modeling of the ACHMI

In this section, system modeling under linear and nonlinear load conditions are both established, an inductive-resistive load is chosen as the linear load and a diode rectifier bridge is considered as the nonlinear load, the complete small-signal model of different load conditions and Floquet theory-based method are introduced in detail through the following parts.

A. System Modeling Under Linear Load Condition

Under linear load condition, the load Z in Fig. 1 is assumed as the linear load (($Z=R+j\omega L_1$)) for the following analysis. The state equations of the power stage are written as:

$$\begin{cases} \dfrac{di_L}{dt} = -\dfrac{1}{L}v_o + \dfrac{1}{L}v_i \\ \dfrac{dv_o}{dt} = \dfrac{1}{C}i_L - \dfrac{1}{C}i_o \\ \dfrac{di_o}{dt} = \dfrac{1}{L_1}v_o - \dfrac{R}{L_1}i_o \end{cases} \tag{9}$$

The state variables containing the small-signal perturbation forms are expressed as:

$$\begin{cases} i_L = \bar{i}_L + \tilde{i}_L \\ v_o = \bar{v}_o + \tilde{v}_o \\ i_o = \bar{i}_o + \tilde{i}_o \end{cases} \tag{10}$$

where $\bar{i}_L$, $\bar{v}_o$, and $\bar{i}_o$ are the hypothetical steady-state operating trajectories points, and $\tilde{i}_L$, $\tilde{v}_o$, and $\tilde{i}_o$ denote the disturbance parts. Substituting (10) into (9), and separating the perturbation components, (9) can be rewritten in the small-signal forms as:

$$\begin{cases} \dfrac{d\tilde{i}_L}{dt} = -\dfrac{1}{L}\tilde{v}_o + \dfrac{1}{L}\tilde{v}_i \\ \dfrac{d\tilde{v}_o}{dt} = \dfrac{1}{C}\tilde{i}_L - \dfrac{1}{C}\tilde{i}_o \\ \dfrac{d\tilde{i}_o}{dt} = \dfrac{1}{L_1}\tilde{v}_o - \dfrac{R}{L_1}\tilde{i}_o \end{cases} \tag{11}$$

where $\tilde{v}_i$ is derived step-by-step in the following parts.

In the control stage, the transfer function between v_α and v_β of the time delay module is $e^{-\tau s}$, and its first-order Pade approximation can be denoted as:

$$\frac{v_\beta(s)}{v_\alpha(s)} = e^{-\tau s} \approx \frac{2-\tau s}{2+\tau s} \tag{12}$$

Then, the differential equation on v_α and v_β is obtained as:

$$2v_\alpha - \tau\frac{dv_\alpha}{dt} = 2v_\beta + \tau\frac{dv_\beta}{dt} \tag{13}$$

Arranging (13), (14) can be obtained:

$$\tau\left(\frac{dv_\alpha}{dt} + \frac{dv_\beta}{dt}\right) = 4v_\alpha - 2(v_\alpha + v_\beta) \tag{14}$$

Setting $v_\alpha+v_\beta = x_1$, where x_1 is regarded as a dummy state variable, hence the differential equation and its small-signal description can be given as (15).

$$\frac{dx_1}{dt} = \frac{4}{\tau}v_\alpha - \frac{2}{\tau}x_1, \quad \frac{d\tilde{x}_1}{dt} = \frac{4}{\tau}\tilde{v}_\alpha - \frac{2}{\tau}\tilde{x}_1 \tag{15}$$

In the SRF for the voltage control, the d-axis error e_d and the q-axis error e_q signals are expressed as:

$$\begin{cases} e_d = -[(\cos\omega_f t)v_\alpha + (\sin\omega_f t)(x_1 - v_\alpha)] \\ e_q = -V_m - [-(\sin\omega_f t)v_\alpha + (\cos\omega_f t)(x_1 - v_\alpha)] \end{cases} \tag{16}$$

Then, equation (16) can be converted into the small-signal forms as:

$$\begin{cases} \tilde{e}_d = -(\cos\omega_f t)\tilde{v}_\alpha - (\sin\omega_f t)(\tilde{x}_1 - \tilde{v}_\alpha) \\ \tilde{e}_q = (\sin\omega_f t)\tilde{v}_\alpha - (\cos\omega_f t)(\tilde{x}_1 - \tilde{v}_\alpha) \end{cases} \tag{17}$$

Supposing $\frac{dx_d}{dt} = e_d$, $\frac{dx_q}{dt} = e_q$, where x_d and x_q are two other dummy state variables, hence (18) and (19) can be obtained.

$$\begin{cases} \dfrac{d\tilde{x}_d}{dt} = \tilde{e}_d = -(\cos\omega_f t)\tilde{v}_\alpha - (\sin\omega_f t)(\tilde{x}_1 - \tilde{v}_\alpha) \\ \dfrac{d\tilde{x}_q}{dt} = \tilde{e}_q = (\sin\omega_f t)\tilde{v}_\alpha - (\cos\omega_f t)(\tilde{x}_1 - \tilde{v}_\alpha) \end{cases} \tag{18}$$

$$i_C^* = i_{C,\alpha}^* = (\cos\omega_f t)(k_p e_d + k_i x_d) - (\sin\omega_f t)(k_p e_q + k_i x_q) \tag{19}$$

where k_p and k_i represent the proportional and integral gains of the PI controllers in voltage loop in SRF and i_c^* is the current reference signal in current regulator.

After performing some mathematical manipulations, (19) can be rewritten as:

$$i_C^* = -k_p v_\alpha + k_i(\cos\omega_f t)x_d - k_i(\sin\omega_f t)x_q \tag{20}$$

and the small-signal representation of (20) can be denoted as:

$$\tilde{i}_C^* = -k_p\tilde{v}_\alpha + k_i(\cos\omega_f t)\tilde{x}_d - k_i(\sin\omega_f t)\tilde{x}_q \tag{21}$$

The modulation signal V_r and its perturbation form are expressed as:

$$V_r = K(i_C^* - i_C), \quad \tilde{V}_r = K(\tilde{i}_C^* - \tilde{i}_C) \tag{22}$$

where K represents the gain of the current loop and i_C is the

This article has been accepted for publication in a future issue of this journal, but has not been fully edited. Content may change prior to final publication. Citation information: DOI 10.1109/TPEL.2019.2930326, IEEE Transactions on Power Electronics

filter capacitor current.

$V_{r,d}$ is denoted as the initial input modulation signal for the HM. Since the control strategy is carried out in a series of PWM periods, hence $V_{r,d}$ is considered to lag $1.5T_s$ behind V_r, including the one cycle computational delay and a half cycle modulation delay. Then, the transfer function on the variable V_r and $V_{r,d}$, as well as its first-order Pade approximation can be written as:

$$\frac{V_{r,d}(s)}{V_r(s)} = e^{-1.5sT_s} \approx \frac{2-1.5T_s s}{2+1.5T_s s} \tag{23}$$

Transforming (23) into the time domain, (24) can be obtained:

$$2V_r - 1.5T_s \cdot \frac{dV_r}{dt} = 2V_{r,d} + 1.5T_s \cdot \frac{dV_{r,d}}{dt} \tag{24}$$

Rearranging (24), it yields that:

$$1.5T_s\left(\frac{dV_{r,d}}{dt} + \frac{dV_r}{dt}\right) = 4V_r - 2(V_r + V_{r,d}) \tag{25}$$

Setting $V_r + V_{r,d} = x_2$, where x_2 is denoted as the fourth dummy state variable, equation (25) and its small-signal form can be written as:

$$\frac{dx_2}{dt} = \frac{4}{1.5T_s}V_r - \frac{2}{1.5T_s}x_2, \quad \frac{d\tilde{x}_2}{dt} = \frac{4}{1.5T_s}\tilde{V}_r - \frac{2}{1.5T_s}\tilde{x}_2 \tag{26}$$

The filter capacitor current and its small-signal expression are derived as:

$$i_C = C\frac{dv_\alpha}{dt} = i_L - i_o, \quad \tilde{i}_C = C\frac{d\tilde{v}_\alpha}{dt} = \tilde{i}_L - \tilde{i}_o \tag{27}$$

Then, $\tilde{v}_i$ can be expressed as:

$$\begin{aligned}\tilde{v}_i &\approx V_{dc}(\tilde{x}_2 - \tilde{V}_r) \\ &= V_{dc}[\tilde{x}_2 + k_p K\tilde{v}_\alpha - k_i K(\cos\omega_f t)\tilde{x}_d + k_i K(\sin\omega_f t)\tilde{x}_q + K\tilde{i}_L - K\tilde{i}_o]\end{aligned} \tag{28}$$

Arranging the above derivations, the complete description of the small-signal model for the ACHMI is derived as:

$$\frac{d\tilde{\mathbf{X}}}{dt} = \mathbf{A}(t)\tilde{\mathbf{X}} \tag{29}$$

where the state vector $\tilde{\mathbf{X}}$ and matrix $\mathbf{A}(t)$ are derived as:

$$\tilde{\mathbf{X}} = [\tilde{i}_L, \tilde{v}_o, \tilde{i}_o, \tilde{x}_1, \tilde{x}_2, \tilde{x}_d, \tilde{x}_q]^T$$

$$\mathbf{A}(t) = \begin{bmatrix} \frac{KV_{dc}}{L} & \frac{k_p KV_{dc}-1}{L} & -\frac{KV_{dc}}{L} & 0 & \frac{V_{dc}}{L} & -\frac{k_i KV_{dc}}{L}(\cos\omega_f t) & \frac{k_i KV_{dc}}{L}(\sin\omega_f t) \\ \frac{1}{C} & 0 & -\frac{1}{C} & 0 & 0 & 0 & 0 \\ 0 & \frac{1}{L_1} & -\frac{R}{L_1} & 0 & 0 & 0 & 0 \\ 0 & \frac{4}{\tau} & 0 & -\frac{2}{\tau} & 0 & 0 & 0 \\ -\frac{4K}{1.5T_s} & -\frac{4k_p K}{1.5T_s} & \frac{4K}{1.5T_s} & 0 & -\frac{2}{1.5T_s} & \frac{4k_i K}{1.5T_s}(\cos\omega_f t) & -\frac{4k_i K}{1.5T_s}(\sin\omega_f t) \\ 0 & \sin\omega_f t - \cos\omega_f t & 0 & -\sin\omega_f t & 0 & 0 & 0 \\ 0 & \sin\omega_f t + \cos\omega_f t & 0 & -\cos\omega_f t & 0 & 0 & 0 \end{bmatrix}$$

From the above modeling process, it can be noticed that the small-signal model under linear load condition is derived around the hypothetical steady state operating trajectories ($\bar{i}_L$, $\bar{v}_o$, $\bar{i}_o$, $\bar{x}_1$, $\bar{x}_2$, $\bar{x}_d$, $\bar{x}_q$), which implies that the differences among the steady-state solutions are neglected, and thus the system stability at the vicinity of all possible steady-state solutions is regarded as identical in the perspective of the obtained small-signal model. In addition, it can be noted that the small-signal model in (29) is periodically time-variant, due to $\mathbf{A}(t) = \mathbf{A}(t+T)$, where the minimal positive period T equals to $2\pi/\omega_f$. Furthermore, the time-variant characteristic of $\mathbf{A}(t)$ is primarily caused by the coordinate transformation for achieving the PI control in the SRF.

As illustrated in [33], such kind of small-signal model can be analyzed by using the Floquet theory and the system stability can be precisely investigated. According to the differential equation theory, the fundamental-solution matrix for (29) are normally expressed as:

$$\Phi(t) = [\varphi_1(t) \quad \varphi_2(t) \quad \varphi_3(t) \quad \varphi_4(t) \quad \varphi_5(t) \quad \varphi_6(t) \quad \varphi_7(t)] \tag{30}$$

where $\varphi_i(t) \in R^7 (i=1, 2, \ldots, 7)$ are the 7 solution vectors of the equation, and (31) is easily obtained.

$$\dot{\mathbf{\Phi}}(t) = \mathbf{A}(t)\mathbf{\Phi}(t) \tag{31}$$

In (31), replacing t into $t+T$, it yields that:

$$\dot{\mathbf{\Phi}}(t+\mathrm{T}) = \mathbf{A}(t+T)\mathbf{\Phi}(t+T) \tag{32}$$

Equation (32) indicates that $\mathbf{\Phi}(t+T)$ is another expression of the fundamental-solution matrix for (31). Moreover, due to the uniqueness of the fundamental-solution matrix, $\mathbf{\Phi}(t)$ and $\mathbf{\Phi}(t+T)$ must be linearly dependent, which can be described as (33):

$$\mathbf{\Phi}(t+T) = \mathbf{H}\mathbf{\Phi}(t) \tag{33}$$

where $\mathbf{H}$ represents the state transition matrix. Letting $\mathbf{\Phi}(0)$ equals to the identity matrix $\mathbf{I}$, (34) can be obtained:

$$\mathbf{H} = \mathbf{\Phi}(T) \tag{34}$$

In practice, $\mathbf{H}$ can be estimated by using numerical methods. Firstly, dividing the interval [0, T] into N_T equivalent sub-intervals, hence the length of each sub-interval can be denoted as:

$$\Delta_T = \frac{T}{N_T} \tag{35}$$

Thus, the k-th sub-interval is presented as $[t_{k-1}, t_k]$, k =1, 2, 3…N_T, where

$$t_{k-1} = (k-1)\Delta_T, \quad t_k = k\Delta_T \tag{36}$$

Employing a sufficiently large number of N_T, $\mathbf{A}(t)$ can be replaced by its average $\bar{\mathbf{A}}_k$ in $[t_{k-1}, t_k]$, which is written as:

$$\bar{\mathbf{A}}_k = \frac{1}{\Delta_T}\int_{t_{k-1}}^{t_k} \mathbf{A}(t)dt \tag{37}$$

Therefore, in the time interval [0, T], $\mathbf{H}$ can be derived as:

$$\mathbf{H} = \prod_{k=1}^{N_T}[\exp(\bar{\mathbf{A}}_k\Delta_T)] \approx \prod_{k=1}^{N_T}[\mathbf{I} + \sum_{i=1}^{N_e}\frac{(\bar{\mathbf{A}}_k\Delta_T)^i}{i!}] \tag{38}$$

where N_e is the expansion number of the exponential terms.

According to differential equation theory, the eigenvalues of $\mathbf{H}$ denoted by λ_F are defined as the Floquet multipliers, which satisfy the determinant equation, as shown in (39).

$$\det(\lambda_F\mathbf{I} - \mathbf{H}) = 0 \tag{39}$$

Furthermore, a criterion can be found in the Floquet theory to illustrate the system stability, which suggests that a system is stable only when all the Floquet multipliers locate in the unit circle in the complex plane, and the Floquet multiplier exiting the unit circle will lead to a bifurcation phenomenon. Specifically, if there is only one real Floquet multiplier moving outside the unit circle at (1, 0), it will result in the pitchfork bifurcation. On the other hand, when Floquet multiplier moving outside the unit circle at (-1, 0), the period-doubling bifurcation would occur. Moreover, if a sole pair of Floquet multipliers (complex conjugate) exits the unit circle, it indicates the Neimark-Sacker bifurcation [33-36].

B. System Modeling Under Nonlinear Load Condition.

Under the nonlinear load condition, the output of the inverter is connected with the diode rectifier bridge load. In

This article has been accepted for publication in a future issue of this journal, but has not been fully edited. Content may change prior to final publication. Citation information: DOI 10.1109/TPEL.2019.2930326, IEEE Transactions on Power Electronics

order to suppress the odd harmonic components in the inverter output voltage, a harmonic control strategy is added into the voltage controller, as shown in Fig. 4.

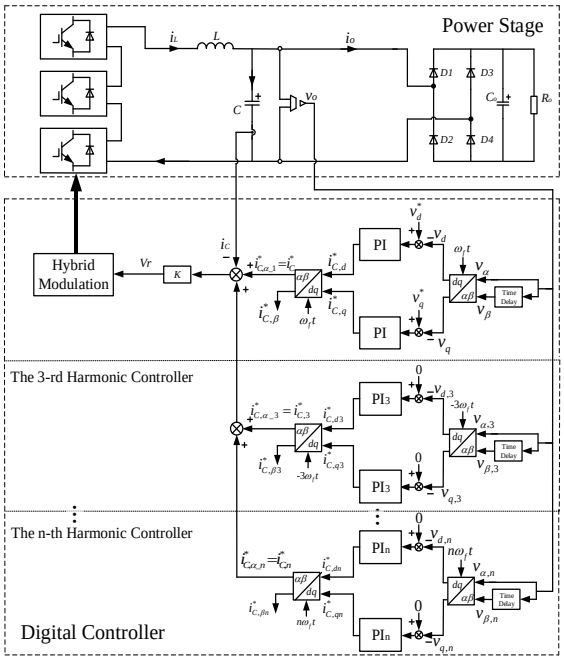

Fig. 4. Block diagram of the ACHMI system under nonlinear load condition.

Under the condition of nonlinear load, i_L and v_o are chosen as state variables, i_o is not considered as a state variable since it could not be written directly with relevant differential equations. The state equation of the main circuit in steady state can be written as:

$$\begin{cases} \dfrac{di_L}{dt} = -\dfrac{1}{L}v_o + \dfrac{1}{L}v_i \\ \dfrac{dv_o}{dt} = \dfrac{1}{C}i_L - \dfrac{1}{C}i_o \end{cases} \tag{40}$$

Then, the state variables containing the small-signal perturbations can be expressed as:

$$\begin{cases} i_L = \overline{i_L} + \tilde{i}_L \\ v_o = \overline{v}_o + \tilde{v}_o \end{cases} \tag{41}$$

where $\overline{i_L}$ and $\overline{v_o}$ are the hypothetical steady-state operating trajectories, and $\tilde{i}_L$ and $\tilde{v}_o$ denote the perturbation parts.

Substituting (41) into (40), and separating the perturbation components, (40) can be rewritten in small-signal form as:

$$\begin{cases} \dfrac{d\tilde{i}_L}{dt} = -\dfrac{1}{L}\tilde{v}_o + \dfrac{1}{L}\tilde{v}_i \\ \dfrac{d\tilde{v}_o}{dt} = \dfrac{1}{C}\tilde{i}_L - \dfrac{1}{C}\tilde{i}_o \end{cases} \tag{42}$$

where $\tilde{v}_i$ and $\tilde{i}_o$ can be obtained by the following parts.

In the control stage, $v_\alpha = v_o$, and the transfer function of the time delay module between v_α and v_β is $e^{-\tau s}$. Still using the first-order Pade approximation instead of $e^{-\tau s}$ and setting $v_\alpha + v_\beta = x_1$, (43) can be easily obtained:

$$\frac{dx_1}{dt} = \frac{4}{\tau}v_\alpha - \frac{2}{\tau}x_1 \tag{43}$$

Considering x_1 as the dummy state variable, its perturbation form can be obtained:

$$\frac{d\tilde{x}_1}{dt} = \frac{4}{\tau}\tilde{v}_\alpha - \frac{2}{\tau}\tilde{x}_1 \tag{44}$$

Since the low-order harmonic components of the output voltage v_o are dominant under the condition of nonlinear rectifier bridge load, only the 3, 5, 7th harmonic control algorithms are considered in the following process.

As shown in Fig. 4, the $dq1$, $dq3$, $dq5$ and $dq7$ are defined as the orthogonal coordinate systems with the rotational speed of ω_f, $-3\omega_f$, $5\omega_f$ and $-7\omega_f$, respectively.

Consistent with the processing method under linear load condition, the d-axis error e_d and the q-axis error e_q signals in $dq1$ coordinate system are expressed as:

$$\begin{cases} e_{d1} = -[(\cos\omega_f t)v_\alpha + (\sin\omega_f t)(x_1 - v_\alpha)] \\ e_{q1} = -V_m - [-(\sin\omega_f t)v_\alpha + (\cos\omega_f t)(x_1 - v_\alpha)] \end{cases} \tag{45}$$

Setting $\frac{dx_{d1}}{dt} = e_{d1}$, $\frac{dx_{q1}}{dt} = e_{q1}$ the perturbation equations and the part of current component in inner loop can be obtained:

$$\begin{cases} \dfrac{d\tilde{x}_{d1}}{dt} = \tilde{e}_{d1} = -(\cos\omega_f t)\tilde{v}_\alpha - (\sin\omega_f t)(\tilde{x}_1 - \tilde{v}_\alpha) \\ \dfrac{d\tilde{x}_{q1}}{dt} = \tilde{e}_{q1} = (\sin\omega_f t)\tilde{v}_\alpha - (\cos\omega_f t)(\tilde{x}_1 - \tilde{v}_\alpha) \end{cases} \tag{46}$$

$$\begin{aligned} i^*_{C,1} &= (\cos\omega_f t)(k_{p1}e_{d1} + k_{i1}x_{d1}) - (\sin\omega_f t)(k_{p1}e_{q1} + k_{i1}x_{q1}) \\ &= -k_{p1}v_\alpha + k_{i1}(\cos\omega_f t)x_{d1} - k_{i1}(\sin\omega_f t)x_{q1} \end{aligned} \tag{47}$$

Separating the perturbation form, it can be written as:

$$\tilde{i}^*_{C,1} = -k_{p1}\tilde{v}_\alpha + k_{i1}(\cos\omega_f t)\tilde{x}_{d1} - k_{i1}(\sin\omega_f t)\tilde{x}_{q1} \tag{48}$$

where k_{p1} and k_{i1} represent the proportional and integral gains of the PI controller in $dq1$.

Similarly, in $dq3$, the error signals of the d- and q-axis are expressed as follows:

$$\begin{cases} e_{d3} = -[(\cos 3\omega_f t)v_\alpha - (\sin 3\omega_f t)(x_1 - v_\alpha)] \\ e_{q3} = -[(\sin 3\omega_f t)v_\alpha + (\cos 3\omega_f t)(x_1 - v_\alpha)] \end{cases} \tag{49}$$

Assuming $\frac{dx_{d3}}{dt} = e_{d3}$, $\frac{dx_{q3}}{dt} = e_{q3}$, it yields that:

$$\begin{cases} \dfrac{d\tilde{x}_{d3}}{dt} = \tilde{e}_{d3} = -(\cos 3\omega_f t)\tilde{v}_\alpha + (\sin 3\omega_f t)(\tilde{x}_1 - \tilde{v}_\alpha) \\ \dfrac{d\tilde{x}_{q3}}{dt} = \tilde{e}_{q3} = -(\sin 3\omega_f t)\tilde{v}_\alpha - (\cos 3\omega_f t)(\tilde{x}_1 - \tilde{v}_\alpha) \end{cases} \tag{50}$$

$$\begin{aligned} i^*_{C,3} &= (\cos 3\omega_f t)(k_{p3}e_{d3} + k_{i3}x_{d3}) + (\sin 3\omega_f t)(k_{p3}e_{q3} + k_{i3}x_{q3}) \\ &= -k_{p3}v_\alpha + k_{i3}(\cos 3\omega_f t)x_{d3} + k_{i3}(\sin 3\omega_f t)x_{q3} \end{aligned} \tag{51}$$

The perturbation form of (51) can be written as:

$$\tilde{i}^*_{C,3} = -k_{p3}\tilde{v}_\alpha + k_{i3}(\cos 3\omega_f t)\tilde{x}_{d3} + k_{i3}(\sin 3\omega_f t)\tilde{x}_{q3} \tag{52}$$

where k_{p3} and k_{i3} are the proportional and integral gains of the PI controller in $dq3$.

In $dq5$ coordinate system, the error signals of d- and q-axis can be described by (53):

$$\begin{cases} e_{d5} = -[(\cos 5\omega_f t)v_\alpha + (\sin 5\omega_f t)(x_1 - v_\alpha)] \\ e_{q5} = -[-(\sin 5\omega_f t)v_\alpha + (\cos 5\omega_f t)(x_1 - v_\alpha)] \end{cases} \tag{53}$$

Setting $\frac{dx_{d5}}{dt} = e_{d5}$, $\frac{dx_{q5}}{dt} = e_{q5}$, (54) and (55) can be obtained:

$$\begin{cases} \dfrac{d\tilde{x}_{d5}}{dt} = \tilde{e}_{d5} = -(\cos 5\omega_f t)\tilde{v}_\alpha - (\sin 5\omega_f t)(\tilde{x}_1 - \tilde{v}_\alpha) \\ \dfrac{d\tilde{x}_{q5}}{dt} = \tilde{e}_{q5} = (\sin 5\omega_f t)\tilde{v}_\alpha - (\cos 5\omega_f t)(\tilde{x}_1 - \tilde{v}_\alpha) \end{cases} \tag{54}$$

$$\begin{aligned} i^*_{C,5} &= (\cos 5\omega_f t)(k_{p5}e_{d5} + k_{i5}x_{d5}) - (\sin 5\omega_f t)(k_{p5}e_{q5} + k_{i5}x_{q5}) \\ &= -k_{p5}v_\alpha + k_{i5}(\cos 5\omega_f t)x_{d5} - k_{i5}(\sin 5\omega_f t)x_{q5} \end{aligned} \tag{55}$$

Separating the perturbation form, it can be written as:

This article has been accepted for publication in a future issue of this journal, but has not been fully edited. Content may change prior to final publication. Citation information: DOI 10.1109/TPEL.2019.2930326, IEEE Transactions on Power Electronics

$$\tilde{i}_{C,5}^{*} = -k_{p5}\tilde{v}_{\alpha} + k_{i5}(\cos 5\omega_f t)\tilde{x}_{d5} - k_{i5}(\sin 5\omega_f t)\tilde{x}_{q5} \quad (56)$$

where k_{p5} and k_{i5} are the proportional and integral gains of the PI controller in $dq5$.

In $dq7$ orthogonal coordinate system, the error signals of d- and q-axis are written as follows:

$$\begin{cases} e_{d7} = -[(\cos 7\omega_f t)v_{\alpha} - (\sin 7\omega_f t)(x_1 - v_{\alpha})] \\ e_{q7} = -[(\sin 7\omega_f t)v_{\alpha} + (\cos 7\omega_f t)(x_1 - v_{\alpha})] \end{cases} \quad (57)$$

Setting $\frac{dx_{d7}}{dt} = e_{d7}$, $\frac{dx_{q7}}{dt} = e_{q7}$, the equation (57) can be modified and the current component can be obtained:

$$\begin{cases} \dfrac{d\tilde{x}_{d7}}{dt} = \tilde{e}_{d7} = -(\cos 7\omega_f t)\tilde{v}_{\alpha} + (\sin 7\omega_f t)(\tilde{x}_1 - \tilde{v}_{\alpha}) \\ \dfrac{d\tilde{x}_{q7}}{dt} = \tilde{e}_{q7} = -(\sin 7\omega_f t)\tilde{v}_{\alpha} - (\cos 7\omega_f t)(\tilde{x}_1 - \tilde{v}_{\alpha}) \end{cases} \quad (58)$$

$$\begin{aligned} i_{C,7}^{*} &= (\cos 7\omega_f t)(k_{p7}e_{d7} + k_{i7}x_{d7}) + (\sin 7\omega_f t)(k_{p7}e_{q7} + k_{i7}x_{q7}) \\ &= -k_{p7}v_{\alpha} + k_{i7}(\cos 7\omega_f t)x_{d7} + k_{i7}(\sin 7\omega_f t)x_{q7} \end{aligned} \quad (59)$$

The small-signal form of (59) can be denoted as:

$$\tilde{i}_{C,7}^{*} = -k_{p7}\tilde{v}_{\alpha} + k_{i7}(\cos 7\omega_f t)\tilde{x}_{d7} + k_{i7}(\sin 7\omega_f t)\tilde{x}_{q7} \quad (60)$$

where k_{p7} and k_{i7} are the proportional and integral gains of the PI controller in $dq7$.

Therefore, the current reference component in the inner loop is obtained as:

$$i_C^{*} = i_{C,1}^{*} + i_{C,3}^{*} + i_{C,5}^{*} + i_{C,7}^{*} \quad (61)$$

Similarly, the perturbation form of current reference can be expressed as:

$$\tilde{i}_C^{*} = \tilde{i}_{C,1}^{*} + \tilde{i}_{C,3}^{*} + \tilde{i}_{C,5}^{*} + \tilde{i}_{C,7}^{*} \quad (62)$$

The modulation signal V_r and its small-signal form can be denoted as:

$$V_r = K(i_C^{*} - i_C), \quad \tilde{V}_r = K(\tilde{i}_C^{*} - \tilde{i}_C) \quad (63)$$

$$\tilde{i}_C = C\frac{d\tilde{v}_{\alpha}}{dt} = \tilde{i}_L - \tilde{i}_o \quad (64)$$

As the same processing method under linear load condition, $V_{r,d}$ is considered to lag $1.5T_s$ behind V_r. Then, the transfer function on the variable V_r and $V_{r,d}$, as well as its first-order Pade approximation can be expressed as:

$$e^{-1.5sT_s} \approx \frac{2 - 1.5T_s s}{2 + 1.5T_s s} \quad (65)$$

Assuming $V_r + V_{r,d} = x_2$, where x_2 is the dummy state variable, the equation in time domain can be expressed as

$$\frac{dx_2}{dt} = \frac{4}{1.5T_s}V_r - \frac{2}{1.5T_s}x_2 \quad (66)$$

$$\frac{d\tilde{x}_2}{dt} = \frac{4}{1.5T_s}\tilde{V}_r - \frac{2}{1.5T_s}\tilde{x}_2 \quad (67)$$

In summary, $\tilde{v}_i$ can be written as:

$$\tilde{v}_i = V_{dc}(\tilde{x}_2 - \tilde{V}_r) = V_{dc}[\tilde{x}_2 - K\tilde{i}_C^{*} + K\tilde{i}_L - K\tilde{i}_o] \quad (68)$$

where $\tilde{i}_o$ can be derived in the following parts.

It is assumed that the output voltage v_o of the inverter is consistent with its reference value in steady state, that is $v_o = v_o^{*} = V_m sin(\omega_f t)$. The simplified circuit of inverter is shown in Fig. 5. According to [37], the output current i_o of inverter is periodic in this case. The precise expression of i_o can be obtained by solving differential equations, and then, i_o is expanded into the Fourier series form to obtain the expression of each current frequency components. However, it is too complex to solve the differential equations. Furthermore, the conduction angles of the diode bridge rectifier are normally calculated through the iterative algorithms like Newton-Raphson method or Gauss-Seidel approach, which are also complicated [38].

To simplify the process of solving current i_o, an alternative approach is adopted in this paper, which is implemented by circuit simulation and numerical fitting software to obtain an accurate expression of i_o and its frequency components.

Firstly, the waveform data of current i_o is acquired in circuit simulation software under the condition that the inverter output voltage is equal to the reference voltage. Then, the waveform data is fitted in the numerical analysis software. Therefore, the precise expression of i_o and its frequency components can be obtained.

Still considering the ACHMI inverter mentioned before, the circuit shown in Fig. 5 are built in PLECS software to simulate the waveform data of i_o in the steady state. In the simulation circuit, L_a=2mH, C_o=2000μF, R_o=50Ω, R_a=4.2Ω, and V_m=32V.

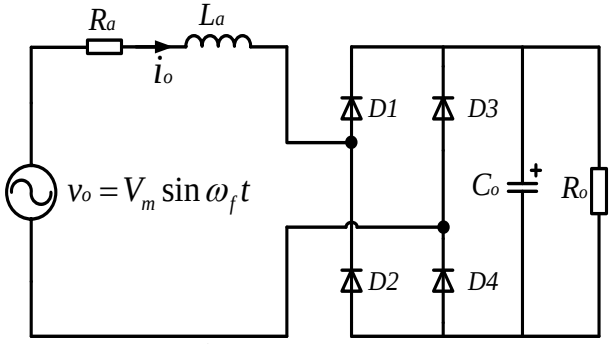

Fig. 5. Simulation circuit for calculating i_o under nonlinear load condition.

The obtained waveform data is fitted in Matlab software. To achieve the maximum approximation of the simulated waveform, the number of sinusoids contained in i_o is set as 8, which is the maximum value in the software. The Trust-Region algorithm and the conventional least squares regression mode are applied to obtain the fitted waveform with 95% confidence bounds. The fitted waveform and the simulation waveform are shown in Fig. 6. The fitted expression of current i_o is written as (69), which is shown at the bottom of this page.

$$\begin{aligned} i_o = {} & 0.7947\sin(\omega_f t - 0.07783) + 0.5197\sin(3\omega_f t + 2.868) + 0.1755\sin(5\omega_f t - 0.4505) + 0.02968\sin(7\omega_f t - 0.08396) \\ & + 0.05144\sin(9\omega_f t + 2.295) + 0.008186\sin(11\omega_f t - 5.305) + 0.02234\sin(13\omega_f t - 1.599) + 0.0117\sin(17\omega_f t - 5.673) \end{aligned} \quad (69)$$

$$\begin{aligned} i_o = {} & 628.401\cdot(\sin\omega_f t)^{17} - 2670.705\cdot(\sin\omega_f t)^{15} + 4671.153\cdot(\sin\omega_f t)^{13} - 4336.19\cdot(\sin\omega_f t)^{11} + 2288.804\cdot(\sin\omega_f t)^{9} - 677.388\cdot(\sin\omega_f t)^{7} \\ & + 104.456\cdot(\sin\omega_f t)^{5} - 7.326\cdot(\sin\omega_f t)^{3} + 0.187\cdot(\sin\omega_f t) + 439.375\cdot(\cos\omega_f t)^{17} - 1867.343\cdot(\cos\omega_f t)^{15} + 3176.381\cdot(\cos\omega_f t)^{13} \\ & - 2730.207\cdot(\cos\omega_f t)^{11} + 1223.9\cdot(\cos\omega_f t)^{9} - 216.702\cdot(\cos\omega_f t)^{7} + 18.898\cdot(\cos\omega_f t)^{5} + 1.479\cdot(\cos\omega_f t)^{3} - 0.752\cdot(\cos\omega_f t) \end{aligned} \quad (70)$$

This article has been accepted for publication in a future issue of this journal, but has not been fully edited. Content may change prior to final publication. Citation information: DOI 10.1109/TPEL.2019.2930326, IEEE Transactions on Power Electronics

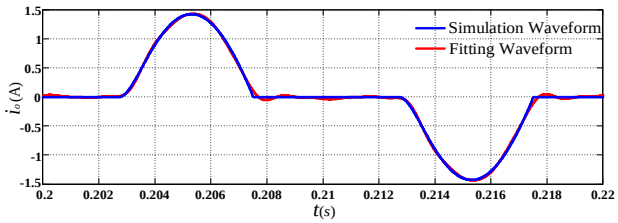

Fig. 6. Comparison of the fitted waveform and simulation waveform of current i_o under the nonlinear load condition.

As shown in Fig. 6, the fitted waveform is consistent with the simulation waveform. Furthermore, the fitting expression of i_o can be expanded and collated, the process is that the current components of each frequency in steady state are rewritten into polynomial forms that only contain $\sin\omega_f t$ and $\cos\omega_f t$ terms. The expression of i_o is rewritten as (70), which is also shown at the bottom of the previous page.

According to the above assumptions, $v_\alpha=v_o=V_m\sin(\omega_f t)$, $v_\beta=-V_m\cos(\omega_f t)$ and $x_1=v_\alpha+v_\beta$. From the perspective of pure mathematics without considering the dimensions of v_α and v_β, the steady state i_o can be expressed as a function of $\sin\omega_f t$ and $\cos\omega_f t$. Therefore, it can be expressed by (71):

$$i_o = f(\sin\omega_f t, \cos\omega_f t) \tag{71}$$

Obviously, i_o can also be written as a function of v_α and v_β in steady state, which can be described as:

$$i_o = f_v(v_\alpha, v_\beta) \tag{72}$$

Under small-signal perturbation, it can be rewritten as:

$$\bar{i}_o + \tilde{i}_o = f_v[(\bar{v}_\alpha + \tilde{v}_\alpha),(\bar{v}_\beta + \tilde{v}_\beta)] \tag{73}$$

where $\bar{i}_o$ and $\tilde{i}_o$ are hypothetical steady state operating points and perturbation components, respectively.

Substituting (73) into (70) and ignoring the higher order (secondary and above) of $\tilde{v}_\alpha$ and $\tilde{v}_\beta$, the perturbation form is written as (74), which is shown at the bottom of this page.

Simplifying and organizing the perturbation component $\tilde{i}_o$, the function of $\tilde{v}_\alpha$ and $\tilde{v}_\beta$ in steady state is expressed as:

$$\tilde{i}_o = K_1\cdot\tilde{v}_\alpha + K_2\cdot\tilde{v}_\beta \tag{75}$$

Therefore, comparing (75) with (74) and bringing V_m value into the equation, the corresponding coefficient K_1 and K_2 can be obtained, as shown in (A1) and (A2) in Appendix A.

Similarly, through integrating the main circuit with the control circuit, the small-signal model under nonlinear load condition with 3, 5, and 7th harmonic control algorithms can be denoted as:

$$\frac{d\tilde{\mathbf{X}}_N}{dt} = \mathbf{A}_N\tilde{\mathbf{X}}_N \tag{76}$$

where the state vector $\tilde{\mathbf{X}}_N$ and matrix $\boldsymbol{A}_N$ are listed in Appendix B.

According to the stability criterion from Floquet theory, the stability region analysis of the ACHMI under linear and linear load conditions can be implemented, which are presented in section IV.

C. Discussion on the System Modeling of the ACHMI in the Grid-Connected Mode

Under grid-connected mode, an LCL filter could be applied to replace the LC filter employed in stand-alone mode, as shown in Fig. 7. In grid-connected mode, the output current i_0 must be controlled to generate the same frequency and phase angle with grid voltage, which is also mainly implemented in SRF. Assuming the grid voltage is $v_g = V_{gm}\cos(\omega_g t + \theta_g)$, and the reference of i_0 is defined as $i_0^* = I_m\cos(\omega_g t + \theta_g)$. Setting $i_o=i_\alpha$, i_α is delayed to generate the virtual current signal i_β. Hence, the *d*-axis and *q*-axis current signals in SRF can be obtained. The angular frequency ω_g and phase θ_g can be obtained by the single-phase PLL, and obviously, ω_g and θ_g are constant for the fixed grid. Selecting the filter inductance current i_L, capacitance voltage v_o, and output current i_o as the state variables, and following the modeling step under linear and nonlinear load conditions, the small signal model of the ACHMI in grid-connected mode can be derived. Similarly, the Floquet theory demonstrated previously can also be used to analyze the system stability.

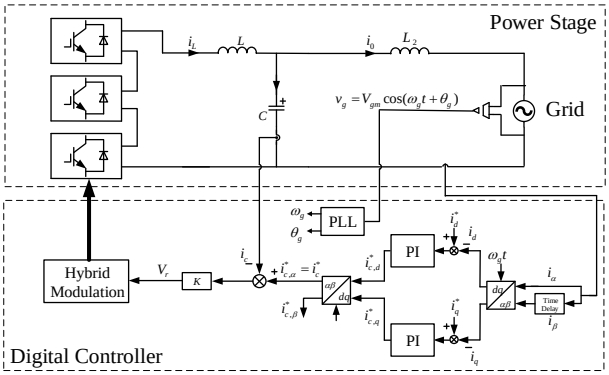

Fig. 7. System structure of the ACHMI system with SRF control loop in grid-connected mode.

IV. Stability Analysis on the Control Parameters

A low-power ACHMI prototype system is considered for the different case studies in this section. The main system parameters are shown in Table I.

TABLE I. System Parameters of the Prototype ACHMI.

Parameter	Symbol	Value
Dc-link voltages of each cell	$V_{dc}/2V_{dc}/6V_{dc}$	4V/8V/24V
Filter inductance	L	2mH
Filter capacitance	C	2.2μF
Switching frequency of the low voltage cell	f_s	10kHz
Fundamental angular frequency	ω_f	100π rad/s
Amplitude of reference voltage	V_m	32V
Resistance of linear load	R	44.2Ω
Inductance of linear load	L_1	2mH
Capacitance of nonlinear load	C_o	2000μF
Resistance of nonlinear load	R_o	50Ω

$$\begin{aligned}\tilde{i}_o = &[\frac{17\cdot628.401}{V_m}\cdot(\sin\omega_f t)^{16} - \frac{15\cdot2670.705}{V_m}\cdot(\sin\omega_f t)^{14} + \frac{13\cdot4671.153}{V_m}\cdot(\sin\omega_f t)^{12} - \frac{11\cdot4336.19}{V_m}\cdot(\sin\omega_f t)^{10} + \frac{9\cdot2288.804}{V_m}\cdot(\sin\omega_f t)^{8} - \frac{7\cdot677.388}{V_m}\cdot(\sin\omega_f t)^{6}\\ &+\frac{5\cdot104.456}{V_m}\cdot(\sin\omega_f t)^{4} - \frac{3\cdot7.326}{V_m}\cdot(\sin\omega_f t)^{2} + \frac{0.187}{V_m}]\cdot\tilde{v}_\alpha\\ &+[\frac{17\cdot439.375}{V_m}\cdot(\cos\omega_f t)^{16} - \frac{15\cdot1867.343}{V_m}\cdot(\cos\omega_f t)^{14} + \frac{13\cdot3176.381}{V_m}\cdot(\cos\omega_f t)^{12} - \frac{11\cdot2730.207}{V_m}\cdot(\cos\omega_f t)^{10} + \frac{9\cdot1223.9}{V_m}\cdot(\cos\omega_f t)^{8} - \frac{7\cdot216.702}{V_m}\cdot(\cos\omega_f t)^{6}\\ &+\frac{5\cdot18.898}{V_m}\cdot(\cos\omega_f t)^{4} + \frac{3\cdot1479}{V_m}\cdot(\cos\omega_f t)^{2} - \frac{0.752}{V_m}]\cdot\tilde{v}_\beta\end{aligned} \tag{74}$$

This article has been accepted for publication in a future issue of this journal, but has not been fully edited. Content may change prior to final publication. Citation information: DOI 10.1109/TPEL.2019.2930326, IEEE Transactions on Power Electronics

A. Stability Analysis Under Linear Load Condition.

The stability regions of three important control parameters in both the voltage and current loop, are investigated in detail with the analysis matrix and Floquet theory, which include the proportional gain k_p and integral gain k_i of the fundamental controllers in the SRF, and the proportional gain K of the current regulator.

Firstly, $\bar{\mathrm{A}}_{\mathrm{k}}$ is calculated for the analysis, as shown in (77).

$$\bar{\mathbf{A}}_k = \begin{bmatrix} \frac{KV_{dc}}{L} & \frac{k_pKV_{dc}-1}{L} & -\frac{KV_{dc}}{L} & 0 & \frac{V_{dc}}{L} & \bar{a}_{16} & \bar{a}_{17} \\ \frac{1}{C} & 0 & -\frac{1}{C} & 0 & 0 & 0 & 0 \\ 0 & \frac{1}{L_1} & -\frac{R}{L_1} & 0 & 0 & 0 & 0 \\ 0 & \frac{4}{\tau} & 0 & -\frac{2}{\tau} & 0 & 0 & 0 \\ -\frac{4K}{1.5T_s} & -\frac{4k_pK}{1.5T_s} & \frac{4K}{1.5T_s} & 0 & -\frac{2}{1.5T_s} & \bar{a}_{56} & \bar{a}_{57} \\ 0 & \bar{a}_{62} & 0 & \bar{a}_{64} & 0 & 0 & 0 \\ 0 & \bar{a}_{72} & 0 & \bar{a}_{74} & 0 & 0 & 0 \end{bmatrix} \quad (77)$$

where the matrix elements are given in Appendix C.

To achieve a tradeoff between the accuracy of analysis and computational burden, N_T=1500 and N_e=5 are set in the Matlab programs to identify the stability regions, which is determined by the Floquet multipliers. In order to obtain the complete analysis results, four typical values of K, 0.5, 1, 2, and 4 are considered for the analysis of the stability regions about k_p and k_i, which are shown in Fig. 8.

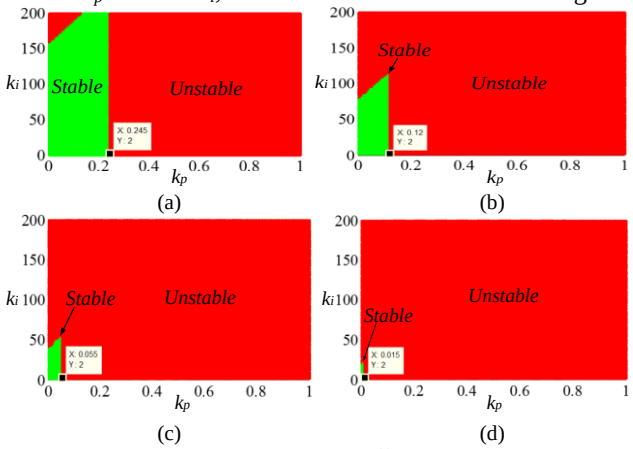

Fig. 8. Stability regions on k_p and k_i under different K, which are obtained by the small-signal model under linear load condition. (a) K=0.5; (b) K=1; (c) K=2; (d) K=4.

As shown in Fig. 8, the green zones represent the k_p and k_i that ensure all Floquet multipliers located in the unit circle of the complex plane, which indicates the stable operating states of the multilevel inverter system. The red areas are formed by the k_p and k_i that cause unstable operating states of the system, given that they make the Floquet multipliers lie on or outside the unit circle. It can be also observed that, a larger K normally causes a smaller stability region on k_p and k_i.

To further verify the small-signal model under linear load condition and reveal the respective effect of k_p, k_i and K on the system stability, three scenarios are taken into consideration according to Fig. 8, which includes:

(i) k_p increases under the condition of K=1 and k_i=20;

(ii) k_i increases under the condition of K=1 and k_p=0.05;

(iii) K increases under the condition of k_p=0.05 and k_i=20.

The obtained results are presented in Fig. 9, Fig. 10, and Fig. 11, respectively.

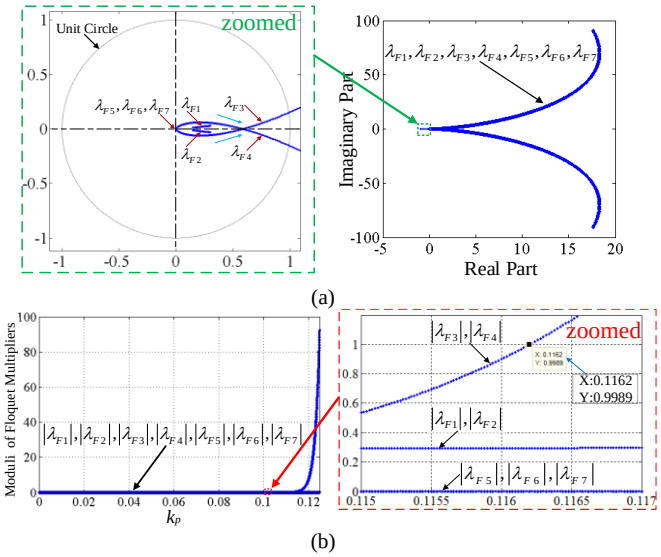

Fig. 9. Loci and moduli of the Floquet multipliers with k_p increase when k_i=20 and K=1 under the linear load condition. (a) Loci of the Floquet multipliers; (b) Moduli of the Floquet multipliers.

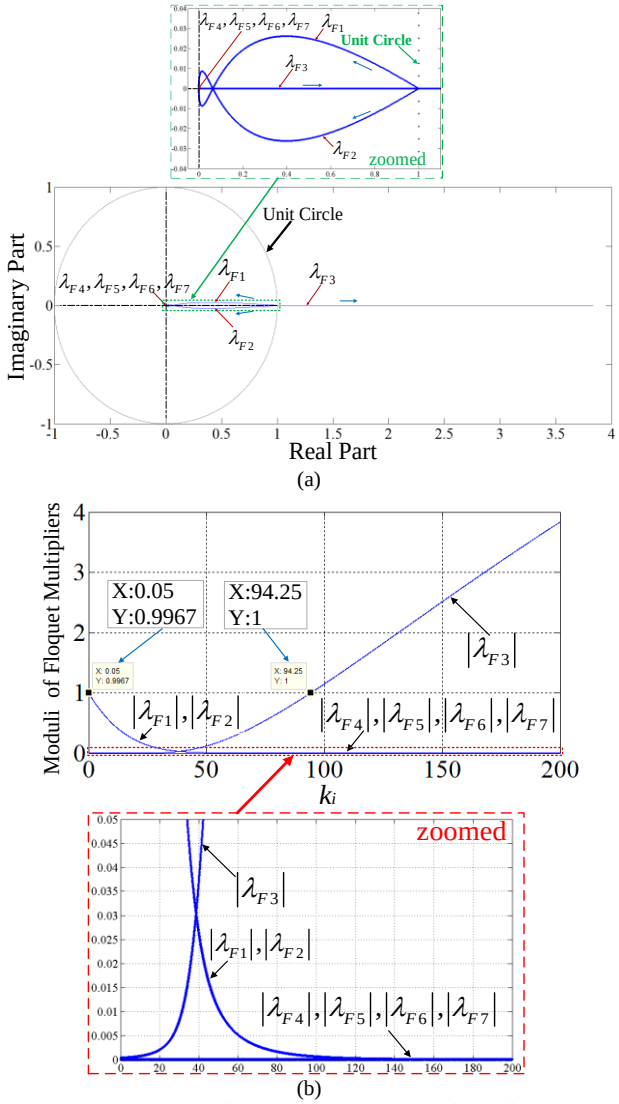

Fig.10. Loci and moduli of the Floquet multipliers for different k_i when k_p=0.05 and K=1 under the linear load condition. (a) Loci of the Floquet multipliers; (b) Moduli of the Floquet multipliers.

Fig. 9 shows the loci and moduli of the Floquet multipliers when k_i=20 and K=1, and k_p increases from 0.001 to 0.125. It

This article has been accepted for publication in a future issue of this journal, but has not been fully edited. Content may change prior to final publication. Citation information: DOI 10.1109/TPEL.2019.2930326, IEEE Transactions on Power Electronics

can be observed that, in the studied range of k_p, the Floquet multipliers λ_{F5}, λ_{F6} and λ_{F7} always stay around the original point (0, 0). The Floquet multipliers λ_{F1} and λ_{F2} constitute a pair of complex conjugate, which move inside the unit circle with the increase of k_p. However, Floquet multiplier λ_{F3} and λ_{F4} move from (0, 0) toward the outside of the unit circle as another pair of complex conjugate, and exit the unit circle when k_p>0.1162. Therefore, it is distinct that when k_i=20 and K=1, the multilevel inverter system would move to the unstable states when k_p is larger than 0.1162, through the Neimark-Sacker bifurcation state where k_p is equal to 0.1162.

The loci and moduli of the Floquet multipliers when k_i varies under k_p=0.05 and K=1 are presented in Fig. 10. As it can be seen, in the studied interval [1, 200], the increase of k_i exerts a slight effect on the Floquet multipliers λ_{F4}, λ_{F5}, λ_{F6} and λ_{F7}, since they remain around the original point (0, 0) in the full studied range of k_i. The Floquet multipliers λ_{F1} and λ_{F2} move from the vicinity of the point (1, 0) in the unit circle to (0, 0) as the complex conjugate. λ_{F3} moves on the real axis, from (0, 0) towards outside the unit circle, and when k_i>94.25, it exit the unit circle through the point (1, 0). It can be subsequently concluded that, the system would operate into the pitchfork bifurcation state from the stable state when k_i increases to 94.25, and then it becomes unstable when k_i is greater than 94.25.

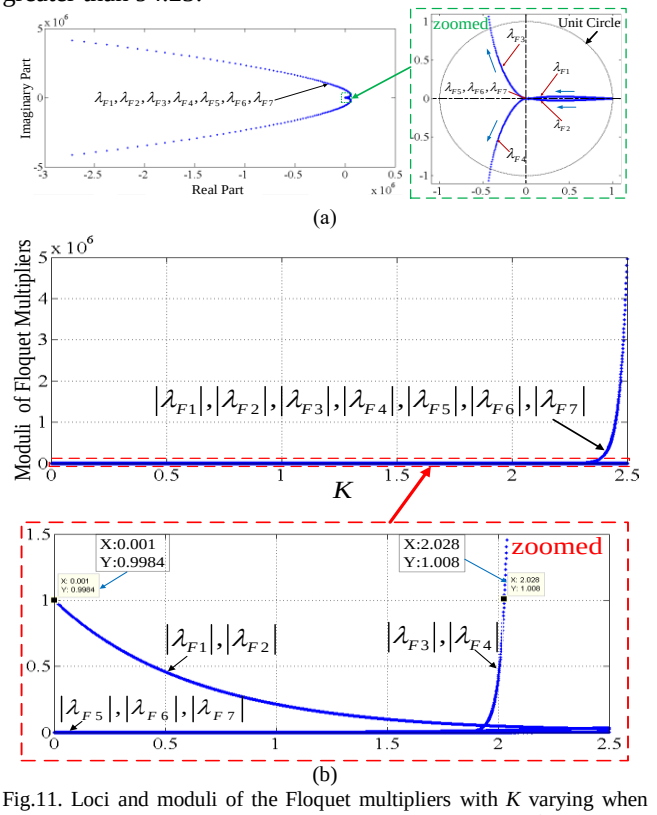

(a)

(b)

Fig.11. Loci and moduli of the Floquet multipliers with K varying when k_p=0.05 and k_i=20 under the linear load condition. (a) Loci of the Floquet multipliers; (b) Moduli of the Floquet multipliers.

The results for the third scenario that K varies under k_p=0.05 and k_i =20 are presented in Fig. 11. It can be observed that, the Floquet multipliers λ_{F5}, λ_{F6} and λ_{F7} keep close to the original point (0, 0), which are unaffected by the change of K. The Floquet multipliers λ_{F1} and λ_{F2} move in the form of complex conjugate, from inside of the unit circle around the point (1, 0) to the original point (0, 0). As other pairs of conjugate complex Floquet multipliers, λ_{F3} and λ_{F4} move towards the outside of the unit circle, from the original point (0, 0), and they arrive at the unit circle when K reaches 2.028. Thus, the system is stable when K<2.028, under the condition of k_p=0.05 and k_i=20, then it goes into the Neimark-Sacker bifurcation state at the critical point where K=2.028, and finally it becomes totally unstable when K exceeds 2.028.

B. Stability Analysis Under Nonlinear Load Condition.

Obviously, the analysis matrix A_N in (76) under nonlinear load condition is also periodically time-variant. For reducing the computational burden, N_T=1000 and N_e=5 are set in the Matlab programs to identify the stability regions determined by the Floquet multipliers.

Since the system small-signal model under nonlinear load condition contains nine control parameters, i.e., k_{p1}, k_{p3}, k_{p5}, k_{p7}, k_{i1}, k_{i3}, k_{i5}, k_{i7} and K, which is too complex to analyze the effect of those parameters on the system stability simultaneously. Moreover, the effects of k_p, k_i, and K on the system stability have been analyzed in detail under linear load condition. Therefore, in order to simplify the theoretical analysis, only the fundamental and 3rd order harmonic control algorithms are considered in the stability analysis for the ACHMI system.

Based on these assumptions, the corresponding small-signal can be separated from the complete model in (76), and $\overline{\mathbf{A}_{N3}}$ is calculated through the same method used in linear load condition, and the matrix $\overline{\mathbf{A}_{N3}}$ is listed in Appendix D.

According to the stability regions and fundamental parameters analyzed in Fig. 8, the stability regions of k_{p3} and k_{i3} are obtained under the condition of four different sets of parameters k_p, k_i and K, as shown in Fig. 12.

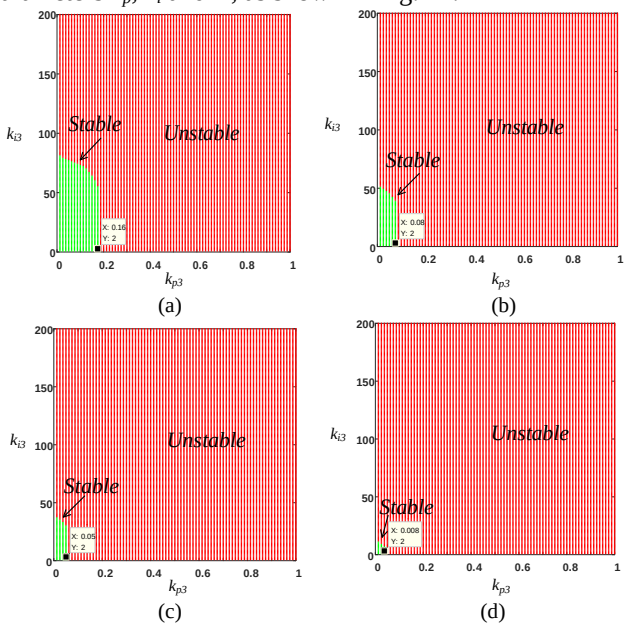

(a) (b) (c) (d)

Fig. 12. Stability regions on k_{p3} and k_{i3} under different sets of fundamental frequency controller parameters. (a) k_p=0.05, k_i=20, K=0.5; (b) k_p=0.05, k_i=20, K=1; (c) k_p=0.12, k_i=20, K=1; (d) k_p=0.12, k_i=80, K=1.

In Fig. 12, the green zones also indicate the stable operating states of the multilevel inverter system, while the red areas represent unstable operating states. It can be observed that, with a large stability region of the fundamental controller (K=0.5), the third harmonic controller also has a large stability region. However, when the fundamental controller has a small stability region (K=1), the stability region of the third order harmonic controller decreases. When the stability region of fundamental controller is fixed (K=1), the stability region of the third harmonic controller varies a little with the achievement of maximum k_p, but once

This article has been accepted for publication in a future issue of this journal, but has not been fully edited. Content may change prior to final publication. Citation information: DOI 10.1109/TPEL.2019.2930326, IEEE Transactions on Power Electronics

k_i also achieve the maximum value, the stability region of the third harmonic controller is much smaller. It suggests that a large stability region of fundamental controller results in a large stability region of the third harmonic controller, and critically stable parameters of the fundamental controller determine a small stability region of the harmonic controller.

To further verify the analysis method and study the effect of k_{p3} and k_{i3} on the system stability, two different scenarios are also taken into consideration under the condition of k_p=0.05, k_i=20, and K=1 according to Fig. 12.

(iv) k_{p3} increases under the condition of k_{i3}=20;

(v) k_{i3} increases under the condition of k_{p3}=0.04;

The obtained results are presented in Fig. 13, and Fig. 14.

As shown in Fig. 13, the Loci and moduli of the Floquet multipliers are presented when k_{p3} increases from 0.001 to 0.1. It can be observed that, in the studied range of k_{p3}, the Floquet multipliers λ_{F3} and λ_{F4} always stay around the original point (0, 0), λ_{F5} and λ_{F6} stay close to the unit circle but never move outside. The Floquet multipliers λ_{F7} and λ_{F8} move inside the unit circle with the increase of k_{p3}, which constitute a pair of complex conjugate. λ_{F1} and λ_{F2} are other pair of Floquet multipliers, and they move from (0, 0) toward the outside of the unit circle, and exit the unit circle when k_{p3}>0.079. It demonstrates that when k_{p3} is larger than 0.079, the system would move to the unstable states under the condition of k_{i3}=20, and the system would operate into Neimark-Sacker bifurcation state when k_{p3} is equal to 0.079.

The loci and moduli of the Floquet multipliers when k_{i3} varies under k_{p3}=0.04 are shown in Fig. 14. As it can be seen, in the studied interval [1, 200], the increase of k_{i3} exerts a slight effect on the Floquet multipliers λ_{F5}, λ_{F6}, λ_{F7} and λ_{F8}, since they remain around the original point (0, 0) in the full studied range of k_{i3}. The Floquet multipliers λ_{F3} and λ_{F4} move inside the unit circle as the complex conjugate with the increase of k_{i3}. Another pair of Floquet multipliers λ_{F1} and λ_{F2} move towards the outside of the unit circle when k_{i3} reaches 50. It can be subsequently concluded that, the system is stable when k_{i3}<50, under k_{p3}=0.04, then it goes into the Neimark-Sacker bifurcation state at the critical point that k_{i3}=50, and finally it becomes totally unstable when k_{i3} is greater than 50.

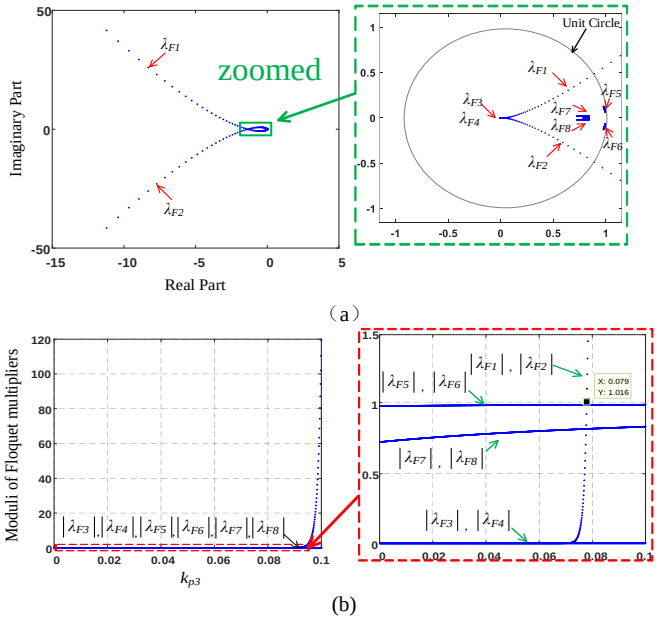

Fig. 13. Loci and moduli of the Floquet multipliers with k_{p3} increase when k_{i3}=20 under nonlinear load condition. (a) Loci of the Floquet multipliers; (b) Moduli of the Floquet multipliers.

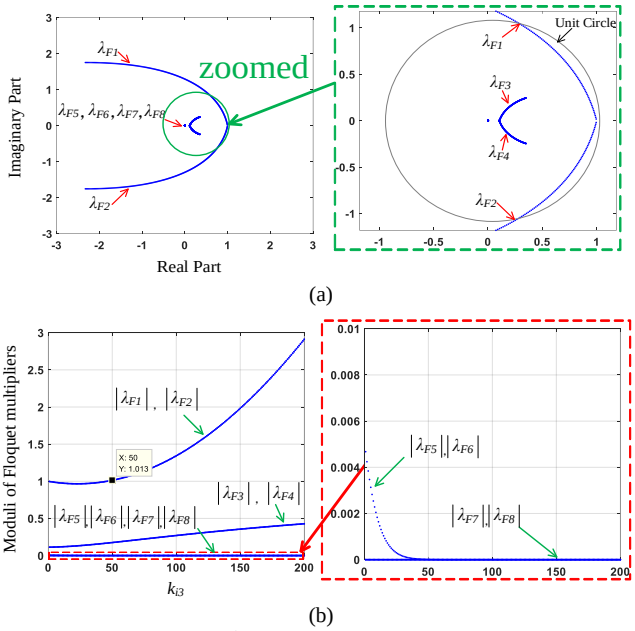

Fig.14. Loci and moduli of the Floquet multipliers with k_{i3} varying when k_{p3}=0.04 under nonlinear load condition. (a) Loci of the Floquet multipliers; (b) Moduli of the Floquet multipliers.

C. Discussion on Control Parameters Selection.

With the above stability analysis under different load conditions, the fundamental and harmonic control parameters in voltage loop and proportional gain of the current loop can be properly selected according to the stability region of parameters.

For the fundamental control parameters k_p and k_i in the SRF, and the proportional gain K of the current regulator, the selection ranges of each parameters are determined by the location of Floquet multipliers, which can be obtained from analysis matrix $\bar{A}_k$. When the Floquet multiplier moves outside the unit circle, it represents the parameters values will cause the instability of the system. Hence, the stability region that makes Floquet multipliers within the unit circle would affect the selection range of control parameters.

Similarly, as for the harmonic control parameters, the location of Floquet multipliers determines the stability region, which can be analyzed by analysis matrix $\bar{A}_N$. Only those parameters within the stability region are suitable for the harmonic controller under nonlinear load condition, hence the stable operation of the ACHMI system can be ensured.

V. Experimental Results and Discussions

A reduced-scale ACHMI prototype is built in accordance with the parameters in Table I to verify the theoretical analysis results, as shown in Fig. 15. The dc-link voltages of the H-bridge cells are provided by three separate programmable DC power supplies. The voltage sensor HPT205A and current sensor ACS712ELCTR-05B-T are employed for measurement, and the control strategy is carried out in the digital controller DSP TMS320F28335. The time-domain waveforms are recorded by using a RIGOL digital oscilloscope. The experimental results under different load conditions are presented as follows.

The transient waveforms in response to turning on the system is first given in Fig. 16. It can be observed that the ACHMI reaches the new steady state in less than a half fundamental cycle, showing a quite fast dynamic response.

This article has been accepted for publication in a future issue of this journal, but has not been fully edited. Content may change prior to final publication. Citation information: DOI 10.1109/TPEL.2019.2930326, IEEE Transactions on Power Electronics

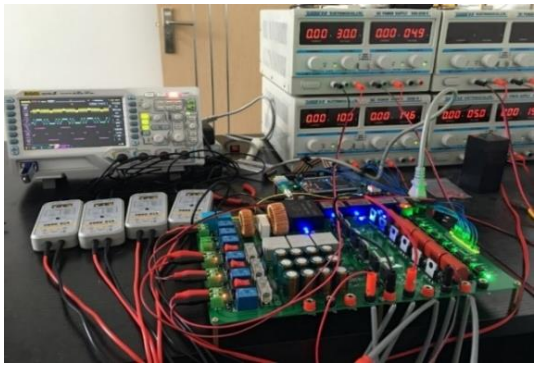

Fig. 15. Photo of the experimental setup using the proposed reduced-scale ACHMI prototype.

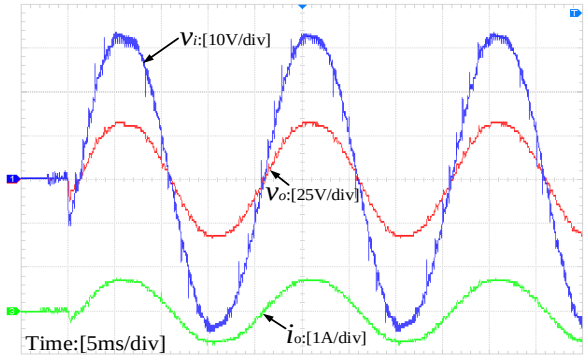

Fig. 16. Transient waveforms when turning on the ACHMI system.

A. Experimental Results Under Linear Load Condition

Fig. 17 shows the steady-state waveforms under the linear load condition for four typical k_p when k_i=20 and K=1, corresponding to the scenario (i) in Section IV. It is evident that the filter capacitor voltage v_o is periodic and sinusoidal when k_p=0.08, which indicates that the ACHMI is stable. However, when k_p=0.1, the waveforms of v_o become slightly distorted, which demonstrates that the ACHMI is marginally stable. Furthermore, when k_p increase to 0.12 and 0.14, the waveform of v_o is remarkably distorted, which suggests that ACHMI system is oscillating. It is obvious that when k_p increases, the stability margin of the multilevel inverter system decreases gradually. In addition, the critical point of k_p located at the range of [0.1, 0.12] can be seen to cause the obvious instability of the system, which is consistent with the theoretical estimation of bifurcation state of 0.1162.

The steady-state waveforms when k_i varies under k_p=0.05 and K=1 are presented in Fig. 18 to validate the analysis of the scenario (ii) in Section IV. It is shown that the waveforms deteriorate with the increase of k_i from 74 to 104, it demonstrates that the multilevel inverter system moves progressively into the unstable states. The distinct distortion in the waveforms is first observed when k_i reaches 94, which indicates the ACHMI is nearly critical stable. However, when k_i=104, a noticeable oscillation is observed, which coincides with the theoretical analysis that ACHMI becomes unstable when k_i is greater than the critical point of 94.25.

Fig. 19 presents the steady-state waveforms for the analysis of scenario (iii) in Section IV, where K varies under the condition of k_p=0.05 and k_i=20. As shown in Fig. 19, the performance degradation is observed when K increases, it indicates that the system become unstable gradually, which is similar to the results in Fig. 17 and Fig. 18. Furthermore, little distortion first appears in waveforms when K is less than 1.8, but when K=2.2, the waveforms are remarkably distorted, which validates the theoretical result that a K greater than 2.028 will result in instabilities of the ACHMI system.

B. Experimental Results Under Nonlinear Load Condition

The steady-state waveforms under nonlinear load condition for different k_{p3} when k_{i3}=20 is presented in Fig. 20. which is consistent with scenario (iv) in Section IV. As shown in Fig. 20(a), when k_{p3}=0.06, which is lower than the critical value 0.079, the waveform of load voltage v_o is sinusoidal and periodic with less distortion. The 3-rd, 5-th and 7-th harmonic components are effectively reduced. Fig. 20(b) presents that when k_{p3} = 0.09, the waveform of v_o has large distortion and high harmonic oscillation can be observed, which is consistent with the theoretical analysis result that the ACHMI system is unstable when k_{p3} of the harmonic controller is greater than the critical value 0.079.

Fig. 21 shows the steady-state waveforms under nonlinear load condition for different k_{i3} under the condition of k_{p3}=0.04, which is consistent with scenario (v) in Section IV. It can be seen from Fig. 21(a) that when k_{i3}=40, which is lower than the critical value 50, the waveform of v_o is sinusoidal with less harmonic components. The odd harmonic components are also suppressed. It suggests that the system is operating in the stable state. However, as shown in Fig. 21(b), when k_{i3}=60, noticeable oscillation and increasing harmonic components are observed in the waveforms of v_o, which verifies the theoretical analysis that a k_{i3} of 3-th harmonic controller larger than 50 will cause the ACHMI system oscillation.

VI. Extension to High Power Applications

The small-signal model and stability analysis mentioned above are studied based on the reduced-scaled ACHMI prototype. However, the analytical model and stability analysis in the previous sections can be extended to ACHMI system with higher power rating in the medium voltage applications, for instance, the 3.3kV, 6kV, 10kV distribution systems. With the different parameter settings, the proposed stability analysis method can be used to study the stability characteristics of different ACHMI system.

With the development of fabrication process for Silicon Carbide (SiC) devices, two typical SiC devices, 15-kV SiC IGBT and 10-kV SiC MOSFET can be applied in the medium-voltage and high-voltage converter system [39]. SiC devices possess higher safe operating junction temperature, higher efficiency, and lower switching loss than Silicon (Si) devices [40]. Since the highest voltage rating of Si IGBT is 6.5kV [41], it is possible to realize higher voltage rating and high-power density applications by using SiC devices instead of Si devices in series. Thus, to optimize the comprehensive utilization of different semiconductor devices, hybrid power stage for medium-voltage system both applying Si and SiC devices has been studied and employed in [42] and [43], which fully utilize the low-switching-loss advantages of SiC devices and the low-cost advantages of Si devices.

In order to verify the validity of the analytical model and stability analysis approach, a 10kV medium-voltage ACHMI system with linear load condition is considered, which has the dc-bus voltage of 1500V, 3000V and 9000V, respectively. In practice, it is possible to achieve those voltage levels through the hybrid power stage, where the low-cost Si devices can be employed in low voltage and medium voltage cells while the high-voltage SiC devices can be used in high voltage H-bridge converter cell. The simulation model of the

This article has been accepted for publication in a future issue of this journal, but has not been fully edited. Content may change prior to final publication. Citation information: DOI 10.1109/TPEL.2019.2930326, IEEE Transactions on Power Electronics

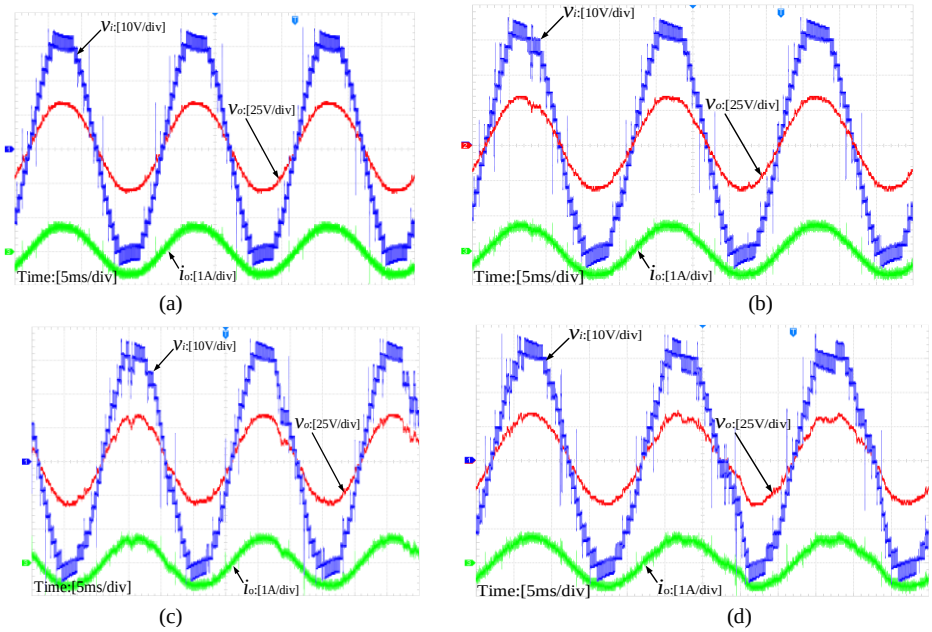

Fig. 17. Steady-state waveforms under linear load condition for different k_p when k_i=20 and K=1. (a) k_p=0.08; (b) k_p=0.1; (c) k_p=0.12; (d) k_p=0.14.

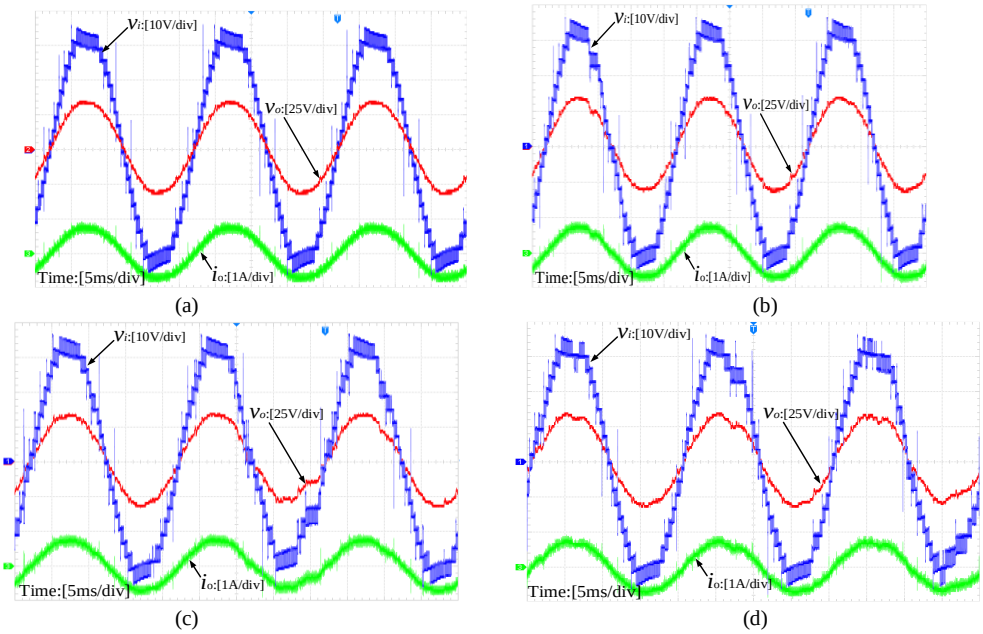

Fig. 18. Steady-state waveforms under linear load condition for different k_i when k_p=0.05 and K=1. (a) k_i=74; (b) k_i=84; (c) k_i=94; (d) k_i=104.

10kV medium-voltage ACHMI system is then established in Matlab/Simulink and the main parameters of the simulation model are listed in Table II.

TABLE II. SYSTEM PARAMETERS OF THE MEDIUM-VOLTAGE ACHMI.

Parameter	Symbol	Value
Dc-link voltages of the H-bridge cells	V_{dc}/2V_{dc}/6V_{dc}	1500V/3000V/9000V
Filter inductance	L	7mH
Filter capacitance	C	100μF
Fundamental angular frequency	ω_f	100π rad/s
Amplitude of reference voltage	V_m	14140V
Resistance of linear load	R	200Ω
Inductance of linear load	L_1	0.5H
proportional gain of voltage loop in SRF	k_p	1.2
integral gain of voltage loop in SRF	k_i	50
proportional gain of the current regulator	K	2

To further reveal the effect of k_p and k_i in voltage loop on the stability of the medium-voltage ACHMI system. Two cases are considered based on the control parameters of the simulation model, which includes:

1). k_p varies under the condition of k_i=50 and K=2.

2). k_i increases under the condition of k_p=1.2 and K=2.

The stability analysis of k_p and k_i are investigated through the small-signal model under linear load condition and the Floquet theory introduced in Section III. However, for the sake of brevity, the detailed analysis process of the loci and moduli of Floquet multipliers are neglected due to space limitations, which is consistent with the theoretical analysis in Section IV. The obtained main results about the stability regions with the variation of k_p and k_i of the medium-voltage ACHMI system are presented as follows:

1). The stability range of k_p is [0.11, 1.72] under the condition of k_i=50 and K=2.

2). The stability range of k_i is [0,122] under the condition of k_p=1.2 and K=2.

This article has been accepted for publication in a future issue of this journal, but has not been fully edited. Content may change prior to final publication. Citation information: DOI 10.1109/TPEL.2019.2930326, IEEE Transactions on Power Electronics

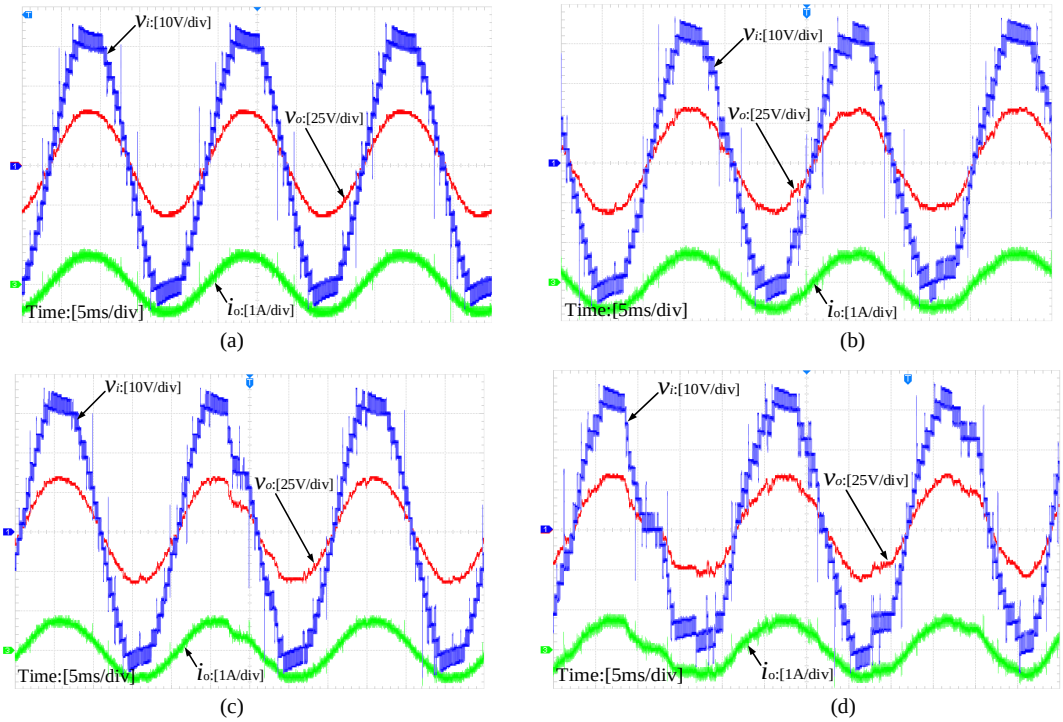

Fig. 19. Steady-state waveforms under linear load condition for different K when k_p=0.05 and k_i=20. (a) K=1.6; (b) K=1.8; (c) K=2; (d) K=2.2.

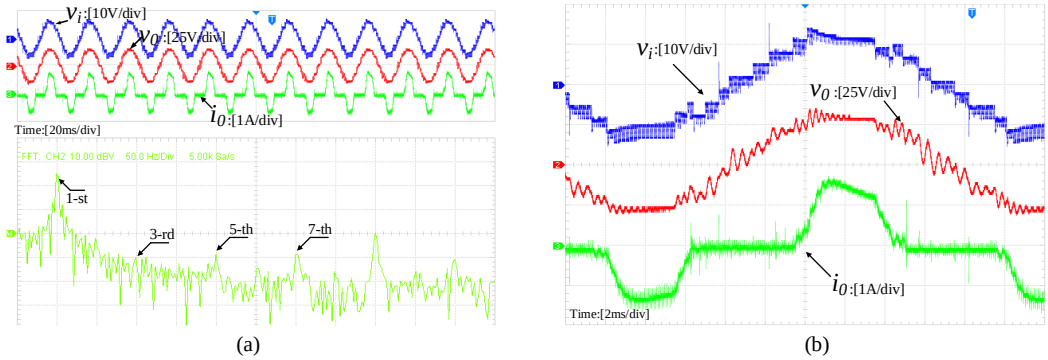

Fig. 20. Steady-state waveforms under nonlinear condition for different k_{p3} when k_{i3}=20. (a) k_{p3}=0.06; (b) k_{p3}=0.09.

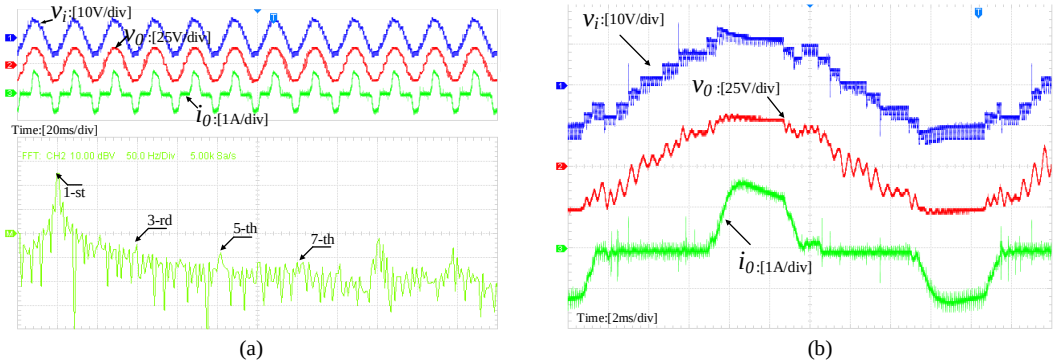

Fig. 21. Steady-state waveforms under nonlinear condition for different k_{i3} when k_{p3}=0.04. (a) k_{i3}=40; (b) k_{i3}=60.

The simulation results of the medium-voltage ACHMI system are presented in Fig. 22 and Fig. 23 to verify the theoretical analysis results.

Fig. 22 shows the steady-state waveforms under the linear load condition for different k_p when k_i=50 and K=2. It can be observed that the filter capacitor voltage v_o is periodic and sinusoidal when k_p=1.5, which indicates that the medium-voltage ACHMI system is stable. However, when k_p=2 exceeds the stability boundary, the waveforms of v_o become distorted. It demonstrates that the medium-voltage ACHMI system is oscillating, which is consistent with the theoretical estimation of stability region of k_p.

The steady-state waveforms when k_i varies under k_p=1.2 and K=2 are presented in Fig. 23 to validate the effect of k_i on the system stability. It is shown that the waveforms of v_o and i_o are both periodic and sinusoidal when k_i=80. However, when k_i =140 exceed 122, a noticeable oscillation is observed in the waveforms, which coincides with the theoretical analysis that the medium-voltage ACHMI system becomes unstable when k_i is greater than the critical point of 122.

This article has been accepted for publication in a future issue of this journal, but has not been fully edited. Content may change prior to final publication. Citation information: DOI 10.1109/TPEL.2019.2930326, IEEE Transactions on Power Electronics

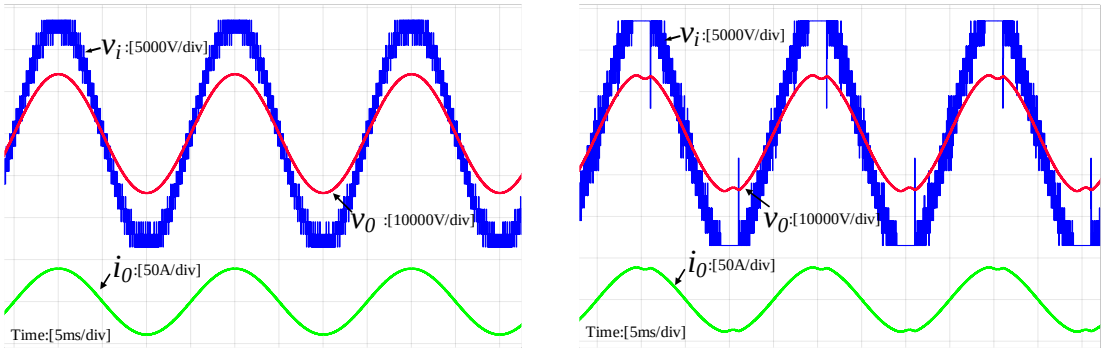

Fig. 22. Simulation waveforms of medium-voltage ACHMI system under linear condition for different k_p when k_i=50 and K=2. (a) k_p=1.5; (b) k_p=2.

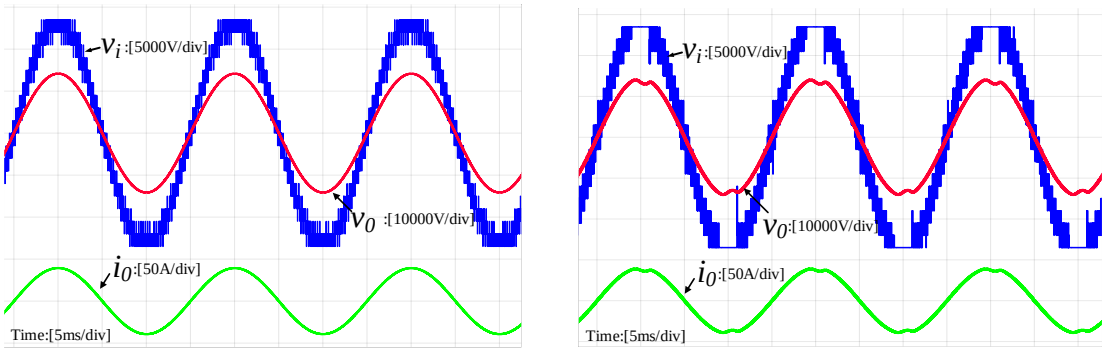

Fig. 23. Simulation waveforms of medium-voltage ACHMI system under linear condition for different k_i when k_p=1.2 and K=2. (a) k_i=80; (b) k_i=140.

The effectiveness of proposed stability analysis method in the 10kV medium-voltage high power ACHMI system has been confirmed by the simulation results. It can be inferred that the proposed stability analysis method can also be extended to analyze the stability characteristics of ACHMI system with different voltage level and power ratings. In addition, by adopting the proposed Floquet theory-based stability analysis method, the control parameters can be properly selected to ensure global stability of ACHMI system.

VII. Conclusion

A small-signal model and the stability analysis method based on Floquet theory of a single-phase ACHMI with the SRF voltage control and hybrid modulation scheme are presented in this paper. The derivation of the small-signal models under different load conditions are conducted around the hypothetical steady-state operating trajectories. It is found that the small-signal model is periodically time-variant due to the SRF voltage control loop, and thus the system stability can be precisely evaluated by the Floquet theory.

The stability analysis of control parameters under linear and nonlinear load conditions is derived through the small-signal model and Floquet theory, hence the parameters of fundamental and harmonic controller of the ACHMI system can be reasonably selected to avoid the instability of system. Besides, the theoretical analysis is validated by experimental results from a reduced-scaled laboratory prototype system. Therefore, the accuracy of the small-signal model and the effectiveness of the Floquet theory-based stability analysis method for ACHMI system operating in stand-alone mode are confirmed. Furthermore, the proposed stability analysis method can be expanded for the analysis of ACHMI system with high-power level, which is verified by the simulation results from the 10kV medium-voltage ACHMI system.

Appendix A

Expressions of coefficient K_1 and K_2.

$$K_1 = 333.84\cdot(\sin\omega_f t)^{16} - 1251.89\cdot(\sin\omega_f t)^{14} + 1897.66\cdot(\sin\omega_f t)^{12} - 1490.56\cdot(\sin\omega_f t)^{10} + 643.73\cdot(\sin\omega_f t)^{8} - 148.18\cdot(\sin\omega_f t)^{6} + 16.321\cdot(\sin\omega_f t)^{4} - 0.6868\cdot(\sin\omega_f t)^{2} + 0.0058 \tag{A1}$$

$$K_2 = 233.42\cdot(\cos\omega_f t)^{16} - 875.317\cdot(\cos\omega_f t)^{14} + 1290.404\cdot(\cos\omega_f t)^{12} - 938.51\cdot(\cos\omega_f t)^{10} + 344.222\cdot(\cos\omega_f t)^{8} - 47.403\cdot(\cos\omega_f t)^{6} + 2.953\cdot(\cos\omega_f t)^{4} + 138.656\cdot(\cos\omega_f t)^{2} - 0.0235 \tag{A2}$$

Appendix B

Expressions of the state vector $\tilde{\mathbf{X}}_N$ and matrix $\boldsymbol{A}_N$

$$\tilde{\mathbf{X}}_N = [\tilde{i}_L \quad \tilde{v}_o \quad \tilde{x}_1 \quad \tilde{x}_2 \quad \tilde{x}_{d1} \quad \tilde{x}_{q1} \quad \tilde{x}_{d3} \quad \tilde{x}_{q3} \quad \tilde{x}_{d5} \quad \tilde{x}_{q5} \quad \tilde{x}_{d7} \quad \tilde{x}_{q7}]^T \tag{B1}$$

This article has been accepted for publication in a future issue of this journal, but has not been fully edited. Content may change prior to final publication. Citation information: DOI 10.1109/TPEL.2019.2930326, IEEE Transactions on Power Electronics

$$\mathbf{A}_N=\begin{bmatrix} \frac{KV_{dc}}{L} & a_{N\_1,2} & \frac{-K_2KV_{dc}}{L} & \frac{V_{dc}}{L} & a_{N\_1,5} & a_{N\_1,6} & a_{N\_1,7} & a_{N\_1,8} & a_{N\_1,9} & a_{N\_1,10} & a_{N\_1,11} & a_{N\_1,12} \\ \frac{1}{C} & \frac{K_2-K_1}{C} & \frac{-K_2}{C} & 0 & 0 & 0 & 0 & 0 & 0 & 0 & 0 & 0 \\ 0 & \frac{4}{\tau} & \frac{-2}{\tau} & 0 & 0 & 0 & 0 & 0 & 0 & 0 & 0 & 0 \\ \frac{-4K}{1.5T_s} & a_{N\_4,2} & \frac{4KK_2}{1.5T_s} & \frac{-2}{1.5T_s} & a_{N\_4,5} & a_{N\_4,6} & a_{N\_4,7} & a_{N\_4,8} & a_{N\_4,9} & a_{N\_4,10} & a_{N\_4,11} & a_{N\_4,12} \\ 0 & a_{N\_5,2} & -\sin\omega_f t & 0 & 0 & 0 & 0 & 0 & 0 & 0 & 0 & 0 \\ 0 & a_{N\_6,2} & -\cos\omega_f t & 0 & 0 & 0 & 0 & 0 & 0 & 0 & 0 & 0 \\ 0 & a_{N\_7,2} & \sin 3\omega_f t & 0 & 0 & 0 & 0 & 0 & 0 & 0 & 0 & 0 \\ 0 & a_{N\_8,2} & -\cos 3\omega_f t & 0 & 0 & 0 & 0 & 0 & 0 & 0 & 0 & 0 \\ 0 & a_{N\_9,2} & -\sin 5\omega_f t & 0 & 0 & 0 & 0 & 0 & 0 & 0 & 0 & 0 \\ 0 & a_{N\_10,2} & -\cos 5\omega_f t & 0 & 0 & 0 & 0 & 0 & 0 & 0 & 0 & 0 \\ 0 & a_{N\_11,2} & \sin 7\omega_f t & 0 & 0 & 0 & 0 & 0 & 0 & 0 & 0 & 0 \\ 0 & a_{N\_12,2} & -\cos 7\omega_f t & 0 & 0 & 0 & 0 & 0 & 0 & 0 & 0 & 0 \end{bmatrix} \tag{B2}$$

$$a_{N\_1,2}=\frac{KV_{dc}}{L}(k_{p1}+k_{p3}+k_{p5}+k_{p7}-K_1+K_2)-\frac{1}{L},\quad a_{N\_1,5}=\frac{-KV_{dc}k_{i1}\cos\omega_f t}{L},\ a_{N\_1,6}=\frac{KV_{dc}k_{i1}\sin\omega_f t}{L} \tag{B3}$$

$$a_{N\_1,7}=\frac{-KV_{dc}k_{i3}\cos(3\omega_f t)}{L},\quad a_{N\_1,8}=\frac{-KV_{dc}k_{i3}\sin(3\omega_f t)}{L},\ a_{N\_1,9}=\frac{-KV_{dc}k_{i5}\cos(5\omega_f t)}{L},\quad a_{N\_1,10}=\frac{KV_{dc}k_{i5}\sin(5\omega_f t)}{L} \tag{B4}$$

$$a_{N\_1,11}=\frac{-KV_{dc}k_{i7}\cos(7\omega_f t)}{L},\ a_{N\_1,12}=\frac{-KV_{dc}k_{i7}\sin(7\omega_f t)}{L},\quad a_{N\_4,2}=\frac{-4K}{1.5T_s}(k_{p1}+k_{p3}+k_{p5}+k_{p7}-K_1+K_2) \tag{B5}$$

$$a_{N\_4,5}=\frac{4Kk_{i1}}{1.5T_s}(\cos\omega_f t),\quad a_{N\_4,6}=\frac{-4Kk_{i1}}{1.5T_s}(\sin\omega_f t),\quad a_{N\_4,7}=\frac{4Kk_{i3}}{1.5T_s}(\cos 3\omega_f t),\ a_{N\_4,8}=\frac{4Kk_{i3}}{1.5T_s}(\sin 3\omega_f t) \tag{B6}$$

$$a_{N\_4,9}=\frac{4Kk_{i5}}{1.5T_s}(\cos 5\omega_f t),\quad a_{N\_4,10}=\frac{-4Kk_{i5}}{1.5T_s}(\sin 5\omega_f t),\ a_{N\_4,11}=\frac{4Kk_{i7}}{1.5T_s}(\cos 7\omega_f t),\quad a_{N\_4,12}=\frac{4Kk_{i7}}{1.5T_s}(\sin 7\omega_f t) \tag{B7}$$

$$a_{N\_5,2}=\sqrt{2}\sin(\omega_f t-\frac{\pi}{4}),\ a_{N\_6,2}=\sqrt{2}\sin(\omega_f t+\frac{\pi}{4}),\quad a_{N\_7,2}=-\sqrt{2}\sin(3\omega_f t+\frac{\pi}{4}),\quad a_{N\_8,2}=-\sqrt{2}\sin(3\omega_f t-\frac{\pi}{4}) \tag{B8}$$

$$a_{N\_9,2}=-\sqrt{2}\sin(5\omega_f t-\frac{\pi}{4}),\quad a_{N\_10,2}=\sqrt{2}\sin(5\omega_f t+\frac{\pi}{4}),\quad a_{N\_11,2}=-\sqrt{2}\sin(7\omega_f t+\frac{\pi}{4}),\ a_{N\_12,2}=-\sqrt{2}\sin(7\omega_f t-\frac{\pi}{4}) \tag{B9}$$

APPENDIX C

Expressions of the elements in (77)

$$\bar{a}_{16}=\frac{-2k_iKV_{dc}}{\omega_f\Delta_t L}\cos[(k-\frac{1}{2})\omega_f\Delta_t]\sin(\frac{\omega_f\Delta_t}{2}),\quad \bar{a}_{17}=\frac{2k_iKV_{dc}}{\omega_f\Delta_t L}\sin[(k-\frac{1}{2})\omega_f\Delta_t]\sin(\frac{\omega_f\Delta_t}{2}) \tag{C1}$$

$$\bar{a}_{56}=\frac{8k_iK}{1.5T_s\omega_f\Delta_t}\cos[(k-\frac{1}{2})\omega_f\Delta_t]\sin(\frac{\omega_f\Delta_t}{2}),\quad \bar{a}_{57}=\frac{-8k_iK}{1.5T_s\omega_f\Delta_t}\sin[(k-\frac{1}{2})\omega_f\Delta_t]\sin(\frac{\omega_f\Delta_t}{2}) \tag{C2}$$

$$\bar{a}_{62}=\frac{-2\sqrt{2}}{\omega_f\Delta_t}\cos[(k-\frac{1}{2})\omega_f\Delta_t+\frac{\pi}{4}]\sin(\frac{\omega_f\Delta_t}{2}),\ \bar{a}_{64}=\frac{-2}{\omega_f\Delta_t}\sin[(k-\frac{1}{2})\omega_f\Delta_t]\sin(\frac{\omega_f\Delta_t}{2}) \tag{C3}$$

$$\bar{a}_{72}=\frac{2\sqrt{2}}{\omega_f\Delta_t}\cos[(k-\frac{1}{2})\omega_f\Delta_t-\frac{\pi}{4}]\sin(\frac{\omega_f\Delta_t}{2}),\quad \bar{a}_{74}=\frac{-2}{\omega_f\Delta_t}\cos[(k-\frac{1}{2})\omega_f\Delta_t]\sin(\frac{\omega_f\Delta_t}{2}) \tag{C4}$$

APPENDIX D

Expressions of the matrix $\overline{\mathbf{A}_{N3}}$

This article has been accepted for publication in a future issue of this journal, but has not been fully edited. Content may change prior to final publication. Citation information: DOI 10.1109/TPEL.2019.2930326, IEEE Transactions on Power Electronics

$$\overline{\mathbf{A}_{N3}}=\begin{bmatrix} \frac{KV_{dc}}{L} & \overline{a_{N3\_12}} & \frac{-K_2KV_{dc}}{L} & \frac{V_{dc}}{L} & \overline{a_{N\_15}} & \overline{a_{N\_16}} & \overline{a_{N\_17}} & \overline{a_{N\_18}} \\ \frac{1}{C} & \frac{K_2-K_1}{C} & \frac{-K_2}{C} & 0 & 0 & 0 & 0 & 0 \\ 0 & \frac{4}{\tau} & \frac{-2}{\tau} & 0 & 0 & 0 & 0 & 0 \\ \frac{-4K}{1.5T_s} & \overline{a_{N3\_42}} & \frac{4KK_2}{1.5T_s} & \frac{-2}{1.5T_s} & \overline{a_{N3\_45}} & \overline{a_{N3\_46}} & \overline{a_{N3\_47}} & \overline{a_{N3\_48}} \\ 0 & \overline{a_{N3\_52}} & \overline{a_{N3\_53}} & 0 & 0 & 0 & 0 & 0 \\ 0 & \overline{a_{N3\_62}} & \overline{a_{N3\_63}} & 0 & 0 & 0 & 0 & 0 \\ 0 & \overline{a_{N3\_72}} & \overline{a_{N3\_73}} & 0 & 0 & 0 & 0 & 0 \\ 0 & \overline{a_{N3\_82}} & \overline{a_{N3\_83}} & 0 & 0 & 0 & 0 & 0 \end{bmatrix} \tag{D1}$$

$$\overline{a_{N3\_12}}=\frac{KV_{dc}}{L}(k_{p1}+k_{p3}-K_1+K_2)-\frac{1}{L},\ \overline{a_{N3\_15}}=\frac{-2k_{i1}KV_{dc}}{\omega_f\Delta_T L}\cos[(k-\frac{1}{2})\omega_f\Delta_T]\sin(\frac{\omega_f\Delta_T}{2}) \tag{D2}$$

$$\overline{a_{N3\_16}}=\frac{2k_{i1}KV_{dc}}{\omega_f\Delta_T L}\sin[(k-\frac{1}{2})\omega_f\Delta_T]\sin(\frac{\omega_f\Delta_T}{2}),\ \overline{a_{N3\_17}}=\frac{-2k_{i3}KV_{dc}}{3\omega_f\Delta_T L}\cos[3(k-\frac{1}{2})\omega_f\Delta_T]\sin(\frac{3\omega_f\Delta_T}{2}) \tag{D3}$$

$$\overline{a_{N3\_18}}=\frac{-2k_{i3}KV_{dc}}{3\omega_f\Delta_T L}\sin[3(k-\frac{1}{2})\omega_f\Delta_T]\sin(\frac{3\omega_f\Delta_T}{2}),\ \overline{a_{N3\_42}}=\frac{-4K}{1.5T_s}(k_{p1}+k_{p3}-K_1+K_2) \tag{D4}$$

$$\overline{a_{N3\_45}}=\frac{8Kk_{i1}}{1.5\omega_f\Delta_T T_s}\cos[(k-\frac{1}{2})\omega_f\Delta_T]\sin(\frac{\omega_f\Delta_T}{2}),\overline{a_{N3\_46}}=\frac{-8Kk_{i1}}{1.5\omega_f\Delta_T T_s}\sin[(k-\frac{1}{2})\omega_f\Delta_T]\sin(\frac{\omega_f\Delta_T}{2}) \tag{D5}$$

$$\overline{a_{N3\_47}}=\frac{8Kk_{i3}}{4.5\omega_f\Delta_T T_s}\cos[3(k-\frac{1}{2})\omega_f\Delta_T]\sin(\frac{3\omega_f\Delta_T}{2}),\ \overline{a_{N3\_48}}=\frac{8Kk_{i3}}{4.5\omega_f\Delta_T T_s}\sin[3(k-\frac{1}{2})\omega_f\Delta_T]\sin(\frac{3\omega_f\Delta_T}{2}) \tag{D6}$$

$$\overline{a_{N3\_52}}=\frac{2\sqrt{2}}{\omega_f\Delta_T}\sin[(k-\frac{1}{2})\omega_f\Delta_T-\frac{\pi}{4}]\sin(\frac{\omega_f\Delta_T}{2}),\ \overline{a_{N3\_53}}=\frac{-2}{\omega_f\Delta_T}\sin[(k-\frac{1}{2})\omega_f\Delta_T]\sin(\frac{\omega_f\Delta_T}{2}) \tag{D7}$$

$$\overline{a_{N3\_62}}=\frac{2\sqrt{2}}{\omega_f\Delta_T}\sin[(k-\frac{1}{2})\omega_f\Delta_T+\frac{\pi}{4}]\sin(\frac{\omega_f\Delta_T}{2}),\ \overline{a_{N3\_63}}=\frac{-2}{\omega_f\Delta_T}\cos[(k-\frac{1}{2})\omega_f\Delta_T]\sin(\frac{\omega_f\Delta_T}{2}) \tag{D8}$$

$$\overline{a_{N3\_72}}=\frac{-2}{3\omega_f\Delta_T}\sin[3(k-\frac{1}{2})\omega_f\Delta_T+\frac{\pi}{4}]\sin(\frac{3\omega_f\Delta_T}{2}),\ \overline{a_{N3\_73}}=\frac{2}{3\omega_f\Delta_T}\sin[3(k-\frac{1}{2})\omega_f\Delta_T]\sin(\frac{3\omega_f\Delta_T}{2}) \tag{D9}$$

$$\overline{a_{N3\_82}}=\frac{-2}{3\omega_f\Delta_T}\sin[3(k-\frac{1}{2})\omega_f\Delta_T-\frac{\pi}{4}]\sin(\frac{3\omega_f\Delta_T}{2}),\ \overline{a_{N3\_83}}=\frac{-2}{3\omega_f\Delta_T}\cos[3(k-\frac{1}{2})\omega_f\Delta_T]\sin(\frac{3\omega_f\Delta_T}{2}) \tag{D10}$$

REFERENCE

[1] J. Chavarría, D. Biel, F. Guinjoan, C. Meza, and J. J. Negroni, "Energy-balance control of PV cascaded multilevel grid-connected inverters under level-shifted and phase-shifted PWMs," *IEEE Trans. Ind. Electron.*, vol. 60, no. 1, pp. 98–111, Jan. 2013.

[2] K. Sano, and M. Takasaki, "A transformerless D-STATCOM based on a multivoltage cascade converter requiring no DC sources," *IEEE Trans. Power Electron.*, vol. 27, no. 6, pp. 2783–2795, Jun. 2012.

[3] J. Dixon, J. Pereda, C. Castillo, and S. Bosch, "Asymmetrical multilevel inverter for traction drives using only one DC supply," *IEEE Trans. Veh. Technol.*, vol. 59, no. 8, pp. 3736–3743, Oct. 2010.

[4] M. F. Kangarlu, and E. Babaei, "A generalized cascaded multilevel inverter using series connection of submultilevel inverters," *IEEE Trans. Ind. Electron.*, vol. 28, no. 2, pp. 625–636, Feb. 2013.

[5] A. Mokhberdoran and A. Ajami, "Symmetric and asymmetric design and implementation of new cascaded multilevel inverter topology", *IEEE Trans. Power Electron.*, vol. 29, no. 12, pp. 6712–6724, Dec. 2014.

[6] H. Akagi, "Multilevel converters:fundamental circuits and systems," *Proceedings of the IEEE*, vol. 105, no.11, pp 2048-2065, Apr. 2017.

[7] S. Daher, J. Schmid, and F. L. M. Antunes, "Multilevel inverter topologies for stand-alone PV systems," *IEEE Trans. Ind. Electron.*, vol. 55, no. 7, pp. 2703–2712, Jul. 2008.

[8] L. G. Franquelo, J. Rodriguez, J. I. Leon, S. Kouro, R. Portillo, and M. A. M. Prats, "The age of multilevel converters arrives," *IEEE Ind. Electron. Mag.*, vol. 2, no. 2, pp. 28–39, Jun. 2008.

[9] M. F. Escalante, J. C. Vannier and A. Arzande, "Flying capacitor multilevel inverters and DTC motor drive applications," *IEEE Trans. Ind Electron.*, vol. 49, no. 4, pp. 809-815, Aug. 2002.

[10] V. Yaramasu, B. Wu and J. Chen, "Model-predictive control of grid-tied four-level diode-clamped inverters for high-power wind energy conversion systems," *IEEE Trans. Power Electron.*, vol. 29, no. 6, pp. 2861-2873, Jun. 2014.

[11] M. A. Perez, S. Bernet, J. Rodriguez, S. Kouro and R. Lizana, "Circuit topologies, modeling, control schemes, and applications of modular multilevel converters," *IEEE Trans. Power Electron.*, vol. 30, no. 1, pp. 4-17, Jan. 2015.

[12] M. Pérez, J. Rodríguez, J. Pontt, S. Kouro, "Power distribution in hybrid multi-cell converter with nearest level modulation," *in Proc. ISIE*, Jun. 2007, pp. 736–741.

[13] M. Rashed, C. Klumpner, and G. Asher, "Repetitive and resonant control for a single-phase grid-connected hybrid cascaded multilevel converter," *IEEE Trans. Power Electron.*, vol. 28, no. 5, pp. 2224–2234, May. 2013.

[14] P. Cortés, A. Wilson, S. Kouro, J. Rodriguez, and H. Abu-Rub, "Model predictive control of multilevel cascaded H-bridge inverters," *IEEE Trans. Power Electron.*, vol. 57, no. 8, pp. 2691–2699, Aug. 2010.

[15] J. A. Juarez-Abad, J. Linares-Flores, E. Guzman-Ramire, and H. Sira-Ramirez, "Generalized proportional intgral tracking controller for a single-phase multilevel cascade inverter: an FPGA implementation," *IEEE Trans. Ind Inform.*, vol. 10, no. 1, pp. 256–266, Feb. 2014.

[16] M. Monfared, S. Golestan, and J. M. Guerrero, "Analysis, design, and experimental verification of a synchronous reference frame voltage

control for single-phase inverters," *IEEE Trans. Ind. Electron.*, vol. 61, no. 1, pp. 258–269, Jan. 2014.

[17] J. I. Leon, S. Vazquez , and L. G. Franquelo, "Multilevel converters: control and modulation techniques for their operation and industrial applications," *Proceedings of the IEEE,* vol. 105, no.11, pp 2066-2081, Aug. 2017.

[18] C. Rech, and J. R. Pinheiro, "Impact of hybrid multilevel modulation strategies on input and output harmonic performances," *IEEE Trans. Power Electron.*, vol. 22, no. 3, pp. 967–977, May. 2007.

[19] C. Rech, and J. R. Pinheiro, "Hybrid multilevel converters: unified analysis and design considerations," *IEEE Trans. Power Electron.*, vol. 54, no. 2, pp. 1092–1104, Apr. 2007.

[20] Y. Han, H. Chen, Z. Li, P. Yang, L. Xu, J. M. Guerrero, "Stability analysis for the grid-connected single-phase asymmetrical cascaded multilevel inverter with SRF-PI current control under weak grid conditions," *IEEE Trans. Power Electron.*, vol. 34, no. 3, pp. 2052–2069, Mar. 2019.

[21] S. Mariethoz, "Systematic Design of High-Performance Hybrid cascaded multilevel inverters with active voltage balance and minimum switching losses," *IEEE Trans. Power Electron.*, vol. 28, no. 7, pp. 3100–3113, Jul. 2013.

[22] H. Abu-Rub, J. Holtz, J. Rodriguez, and Ge Baoming, "Medium-voltage multilevel converters—state of the art, challenges, and requirements in industrial applications," *IEEE Trans. Ind. Electron.*, vol. 57, no. 8, pp. 2581–2596, Aug. 2010.

[23] X. Zhang, and J. W. Spencer, "Study of multisampled multilevel inverters to improve control performance," *IEEE Trans. Power. Electron.*, vol. 27, no. 11, pp. 4409–4416, Nov. 2012.

[24] S. Kouro, B. Wu, Á. Moya, E. Villanueva, P. Correa, and J. Rodr ́guez, "Control of a cascaded H-bridge multilevel converter for grid connection of photovoltaic systems," *in Proc. IECON*, Feb. 2009, pp. 3976–3982.

[25] A. Mortezaei, M. G. Sim ões, A. S. Bubshait, Tiago D. C. Busarello, F. P. Marafão, and A. Al Durra, "Multifunctional control strategy for asymmetrical cascaded H-bridge inverter in microgrid applications," *IEEE Trans. Ind. Appl.*, vol. 53, no. 2, pp. 1538–1551, Mar. 2017.

[26] T. D. C. Busarello, A. Mortezaei, H. K. M. Paredes, A. Al-Durra, J. A. Pomilio, and M. G. Simões, "Simplified small-signal model for output voltage control of asymmetric cascaded H-bridge multilevel inverter," *IEEE Trans. Power Electron.*, vol. 33, no. 4, pp. 3509–3519, Apr. 2018.

[27] J. Sun, "Small-signal methods for AC distributed power systems–A Review," *IEEE Trans. Power Electron.*, vol. 24, no. 11, pp. 2545-2554, Aug. 2009.

[28] G. C. Verghese, J. H. Lang, and Leo. F. Casey, "Analysis of instability in electrical machines," *IEEE Trans. Ind. Appl.*, vol. 22, no. 5, pp. 853–864, Sep. 1986.

[29] V. Salis, A. Costabeber, S. Cox, P. Zanchetta, A. Formentini, "Stability boundary analysis in single-phase grid-connected inverters with PLL by LTP theory," *IEEE Trans. Power Electron.*, vol. 33, no. 5, pp. 4023-4036, May. 2018.

[30] X. Zhang, J. W. Spencer, J. M. Guerrero, "Small-signal modeling of digitally controlled grid-connected inverters with LCL filters," *IEEE Trans. Power Electron.*, vol. 60, no. 9, pp. 3752-3765, Jun. 2013.

[31] H. du T. Mouton , S. M. Cox, B. McGrath, L. Risbo, and B. Putzeys, "Small-signal analysis of naturally-sampled single-edge PWM control loops," *IEEE Trans. Power Electron.*, vol. 33, no. 3, pp. 51–64, Jan. 2018.

[32] Y. Han, X. Fang, P. Yang, C. L. Wang, L. Xu, and J. M. Guerrero, "Stability analysis of digital-controlled single-phase inverter with synchronous reference frame voltage control," *IEEE Trans. Power Electron.*, vol. 33, no. 7, pp. 6333–6349, Jul. 2018.

[33] N. Ali. H, B. Balakumar, *Applied Nonlinear Dynamics: Analytical, Computational, and Experimental Methods*, NY, USA: Wiley-VCH, 1995.

[34] P. Friedmann, C. E. Hammond, and Tze-Hsin Woo, "Efficeient numerical treatment of periopdic systems with application to stability problems," *International Journal for Numerical Methods in Engineering*, vol. 11, no. 7, pp. 1117–1136, Jun 1977.

[35] J. H. Shen, K.C. Lin, S.H. Chen, K.Y. Sze, "Bifurcation and route-to-chaos analysis for Mathieu–Duffing oscillator by the incremental harmonic balance method," *Nonlinear Dynamics*, vol. 52, no. 4, pp. 403–414, Aug 2007.

[36] R. Seydel, *Practical Bifurcation and Stability Analysis: From Equilibrium to Chaos*, 2nd ed., NY, USA: World Press, 1994.

[37] A. Mansoor, W. M. Grady, A. H. Chowdhury, and M. J. Samotyj, "An investigation of harmonics attenuation and diversity among distributed single-phase power electronics loads," *IEEE Trans. Power Del.*, vol. 10, no. 1, pp. 467–473, Jan. 1995.

[38] D. G. Kim, T. Nakajima, Nonmembers, and E. Masada, "Harmonic analysis of a capacitor-filtered rectifier with line impedence," *Elelctron. Commun. Japan Part I, Commun.,* vol. 72, no. 4, pp. 1-9, Apr. 1989.

[39] S. Madhusoodhanan *et al*., "Solid-state transformer and MV grid tie applications enabled by 15 kV SiC IGBTs and 10 kV SiC MOSFETs based multilevel converters," *IEEE Trans. Ind. Appl*., vol. 51, no. 4, pp. 3343-3360, Jul. 2015.

[40] L. Wu, J. Qin, M. Saeedifard, O. Wasynczuk and K. Shenai, "Efficiency evaluation of the modular multilevel converter based on Si and SiC switching devices for medium/high-voltage applications," *IEEE Trans. Electron Devices*., vol. 62, no. 2, pp. 286-293, Feb. 2015.

[41] S. Madhusoodhanan, K. Mainali, A. K. Tripathi, A. Kadavelugu, D. Patel and S. Bhattacharya, "Power loss analysis of medium-voltage three-phase converters using 15-kV/40-A SiC N-IGBT," *IEEE J. Emerg. Sel. Topics Power Electron.*, vol. 4, no. 3, pp. 902-917, Sep. 2016.

[42] Q. Guan *et al*., "An extremely high efficient three-level active neutral-point-clamped converter comprising SiC and Si hybrid power stages," *IEEE Trans. Power Electron.*, vol. 33, no. 10, pp. 8341-8352, Oct. 2018.

[43] Y. Koyama, Y. Nakazawa, H. Mochikawa, A. Kuzumaki, K. Sano and N. Okada, "A transformerless 6.6-kV STATCOM based on a hybrid cascade multilevel converter using SiC devices," *IEEE Trans. Power Electron.*, vol. 33, no. 9, pp. 7411-7423, Sep. 2018.

Yang Han (S'08-M'10-SM'17) received the Ph.D. in Electrical Engineering from Shanghai Jiaotong University (SJTU), Shanghai, China, in 2010.

In 2010, he joined the Department of Power Electronics, School of Mechatronics Engineering, University of Electronic Science and Technology of China (UESTC), Chengdu, China, where since 2013, he has been an Associate Professor. Currently, he is with the Department of Electrical Engineering, School of Mechanical and Electrical Engineering, UESTC. From March 2014 to March 2015, he was a Visiting Scholar with the Department of Energy Technology, Aalborg University, Aalborg, Denmark. He has authored more than 20 ISI-indexed international journal papers, including 3 ESI highly cited paper, 1 ESI hot paper and one book chapter in the area of power electronics, power quality conditioners, and smart grid. He holds 25 issued and nine pending patents. His research interests include the ac/dc microgrids, active distribution networks, power quality, grid-connected converters for renewable energy systems, active power filters, multilevel converters, and static synchronous compensators (STATCOMs).

Dr. Han was a Session Chair for "Emerging Technologies and End-user Systems", "Grid Operation and Management", and "Power Electronics, Control and Protection Systems for Smart Grids" Sessions in IEEE PES Innovative Smart Grid Technologies Asia (ISGT Asia 2019), Chengdu, China, in 2019, for "Microgrid and Distributed Generation" Session in the Symposium on Power Electronics and Electrical Drives (SPEED), Xi'an, China, in 2019, for "Microgrid Optimization and Scheduling" Session in the 2nd International Conference on Power and Renewable Energy, Chengdu, China, in 2017, for "Power Quality Mitigation and Application" Session in the 5th National Conference on Power Quality, Xi'an, China, in 2017, and for "AC/DC, DC/AC Power Converter" Session in the 2016 IPEMC ECCE-Asia, Hefei, China. He was the recipient of the "Academic Talent Award" by UESTC in 2017, and "Baekhyun Award" by the Korean Institute of Power Electronics) in 2016. He was the recipient of the Best Paper Awards from the 34th Annual Conference on Power System and Automation of Chinese Universities in 2018, the Joint Conference of Sichuan Power Supply Society and Chongqing Power Supply Society in 2018, the 6th Asia International Symposium on Mechatronics in 2017, the 5th National Conference on Power Quality in 2017, the Annual Conference of HVDC and Power Electronics Committee of Chinese Society of Electrical Engineers in 2013, and the 4th International Conference on Power Quality in 2008, China. He is an Associate Editor for IEEE ACCESS and Journal of Power Electronics (JPE).

This article has been accepted for publication in a future issue of this journal, but has not been fully edited. Content may change prior to final publication. Citation information: DOI 10.1109/TPEL.2019.2930326, IEEE Transactions on Power Electronics

Xiangyang Lin received the B.S. degree in electrical engineering and automation in 2018 from the University of Electronic Science and Technology of China (UESTC), Chengdu, China, where he is currently working toward the M.S. degree in power electronics and electric drives. His main research interests include stability analysis of inverters and modeling of the renewable-energy generation systems.

Xu Fang received the B.S. degree in electrical engineering and automation in 2015 from the University of Electronic Science and Technology of China (UESTC), Chengdu, China, where he received the M.S. degree in power electronics and electric drives in 2018. His current research interests include system modeling and stability analysis of power electronic converters and microgids, power quality management, and control methods of distributed generation systems.

Lin Xu received the Ph.D. degree in Electrical Engineering from Shanghai JiaoTong University (SJTU), Shanghai, China, in 2011. Currently, she is a Senior Engineering at Sichuan Electric Power Research Institute, State Grid Sichuan Electric Power Company, Chengdu, China. She has co-authored more than 20 journal and conference papers in the area of power electronics and power systems.

Her research interests include power quality, power system analysis and real-time digital simulator (RTDS), flexible Ac transmission systems (FACTS), such as STATCOMs and power quality conditioners (DVRs, APFs). She is an active reviewer for IEEE Transactions on Industrial Electronics, IEEE Transactions on Power Electronics, Electric Power Components and Systems, etc.

Ping Yang received the B.S. in Mechanical Engineering from Shanghai Jiaotong University (SJTU), Shanghai, China, in 1984, and the M. S. in Mechanical Engineering from Sichuan University in 1987, respectively. He is currently a full professor with the School of Mechatronics Engineering, University of Electronic Science and Technology of China (UESTC), Chengdu, China. He was visiting the Victory University, Australia from July 2004 to August 2004, and a visiting scholar with the S. M. Wu Manufacturing Research Center, University of Michigan, Ann Arbor, USA, from August 2009 to February 2010, and was visiting the University of California, Irvine, USA, from October 2012 to November 2012.

His research includes mechatronics engineering, electrical engineering and automation, computer-aided control and instrumentation, smart mechatronics, and detection and automation of mechanical equipment. He has authored more than 60 papers in various journals and international conferences, and several books on mechatronics and instrumentation. He received several provincial awards for his contribution in teaching and academic research. He is currently the Dean of the School of Mechatronics Engineering, UESTC.

Weihao Hu (S'06–M'13–SM'15) received the B.Eng. and M.Sc. degrees from Xi'an Jiaotong University, Xi'an, China, in 2004 and 2007, respectively, both in electrical engineering, and Ph. D. degree from Aalborg University, Denmark, in 2012. He is currently a Full Professor and the Director of Institute of Smart Power and Energy Systems (ISPES) at the University of Electronics Science and Technology of China (UESTC). He was an Associate Professor at the Department of Energy Technology, Aalborg University, Denmark and the Vice Program Leader of Wind Power System Research Program at the same department. His research interests include intelligent energy systems and renewable power generation. He has led/participated in more than 10 national and international research projects and he has more than 130 publications in his technical field. He has been Guest Editor of the IEEE TRANSACTIONS ON POWER SYSTEM Special Section: Enabling very high penetration renewable energy integration into future power systems, and ENERGIES Special Issue: Energy Management in Vehicle–Grid–Traffic Nexus. He was serving as the Technical Program Chair (TPC) for IEEE Innovative Smart Grid Technologies (ISGT) Asia 2019.

Ernane Antônio Alves Coelho received the B.S. degree in electrical engineering from the Federal University of Minas Gerais, Belo Horizonte, Brazil, the M.S. degree from the Federal University of Santa Catarina, Florianopolis, Brazil, and the Ph.D. degree from the Federal University of Minas Gerais in 1987, 1989, and 2000, respectively. In 1989, he joined the Electrical Engineering Faculty at Federal University of Uberlandia, where he is currently a Full Professor. His research interests are Power-factor Correction, PV and Fuel Cell Systems, Microgrid Modelling and Digital Control by microcontrollers and DSP's.

Frede Blaabjerg (S'86–M'88–SM'97–F'03) was with ABB-Scandia, Randers, Denmark, from 1987 to 1988. From 1988 to 1992, he got the PhD degree in Electrical Engineering at Aalborg University in 1995. He became an Assistant Professor in 1992, an Associate Professor in 1996, and a Full Professor of power electronics and drives in 1998. From 2017 he became a Villum Investigator. He is honoris causa at University Politehnica Timisoara (UPT), Romania and Tallinn Technical University (TTU) in Estonia.

His current research interests include power electronics and its applications such as in wind turbines, PV systems, reliability, harmonics and adjustable speed drives. He has published more than 600 journal papers in the fields of power electronics and its applications. He is the co-author of four monographs and editor of ten books in power electronics and its applications.

He has received 31 IEEE Prize Paper Awards, the IEEE PELS Distinguished Service Award in 2009, the EPE-PEMC Council Award in 2010, the IEEE William E. Newell Power Electronics Award 2014, the Villum Kann Rasmussen Research Award 2014 and the Global Energy Prize in 2019. He was the Editor-in-Chief of the IEEE TRANSACTIONS ON POWER ELECTRONICS from 2006 to 2012. He has been Distinguished Lecturer for the IEEE Power Electronics Society from 2005 to 2007 and for the IEEE Industry Applications Society from 2010 to 2011 as well as 2017 to 2018. In 2019-2020 he serves the President of IEEE Power Electronics Society. He is Vice-President of the Danish Academy of Technical Sciences too. He is nominated in 2014-2018 by Thomson Reuters to be between the most 250 cited researchers in Engineering in the world.